UNCLASSIFIED

AD NUMBER: AD0822283
LIMITATION CHANGES
TO: Approved for public release; distribution is unlimited.
FROM: This docment is subject to special export controls; 01 Oct 1967, and each transmittal to foreign governments or foreign nationals may be made only with prior approval of AFWL (WLRE), Kirtland AFB, N.M. 87117. Distribution of this docment is limited because of the technology discussed.
AUTHORITY
ST-A AFWL LTR, 30 NOV 1971

THIS PAGE IS UNCLASSIFIED

AFWL-TR-67-45

AFWL-TR
67-45

AD822283

SHORT-TERM ANNEALING IN SEMICONDUCTOR MATERIALS AND DEVICES

J. W. Harrity and C. E. Mallon
General Dynamics
General Atomic Division
San Diego, California
Contract AF29(601)-7183

TECHNICAL REPORT NO. AFWL-TR-67-45

October 1967

AIR FORCE WEAPONS LABORATORY
Research and Technology Division
Air Force Systems Command
Kirtland Air Force Base
New Mexico

AFWL-TR-67-45

Research and Technology Division
AIR FORCE WEAPONS LABORATORY
Air Force Systems Command
Kirtland Air Force Base
New Mexico

When U. S. Government drawings, specifications, or other data are used for any purpose other than a definitely related Government procurement operation, the Government thereby incurs no responsibility nor any obligation whatsoever, and the fact that the Government may have formulated, furnished, or in any way supplied the said drawings, specifications, or other data, is not to be regarded by implication or otherwise, as in any manner licensing the holder or any other person or corporation, or conveying any rights or permission to manufacture, use, or sell any patented invention that may in any way be related thereto.

This report is made available for study with the understanding that proprietary interests in and relating thereto will not be impaired. In case of apparent conflict or any other questions between the Government's rights and those of others, notify the Judge Advocate, Air Force Systems Command, Andrews Air Force Base, Washington, D. C. 20331.

This document is subject to special export controls and each transmittal to foreign governments or foreign nationals may be made only with prior approval of AFWL (WLRE), Kirtland AFB, N.M. 87117. Distribution of this document is limited because of the technology discussed.

DO NOT RETURN THIS DOCUMENT. RETAIN OR DESTROY.

AFWL-TR-67-45

SHORT-TERM ANNEALING IN SEMICONDUCTOR MATERIALS AND DEVICES

J. W. Harrity

C. E. Mallon

General Dynamics
General Atomic Division
San Diego, California

Contract AF29(601)-7183

TECHNICAL REPORT NO. AFWL-TR-67-45

This document is subject to special export controls and each transmittal to foreign governments or foreign nationals may be made only with prior approval of AFWL (WLRE), Kirtland AFB, N.M. Distribution of this document is limited because of the technology discussed.

FOREWORD

This report was prepared by the Special Effects Laboratory, General Atomic Division, General Dynamics Corporation, San Diego, California, under Contract AF29(601)-7183. The research was performed under Program Element 6.16.46.01.D, Project 5710, Task 16, Subtask RTR1.042, and was funded by the Defense Atomic Support Agency (DASA).

Inclusive dates of research were April 1966 to April 1967. The report was submitted 15 September 1967 by the AFWL Project Officer, Capt Stanley O. Kennedy, Sr., (WLRE).

The contractor's report number is GA-7972.

This report has been reviewed and is approved.

STANLEY O. KENNEDY, SR.
Captain, USAF
Project Officer

WILLIAM N. JACKOMIS
Major, USAF
Chief, Effects Branch

CLAUDE K. STAMBAUGH
Colonel, USAF
Chief, Research Division

AFWL-TR-67-45

ABSTRACT

(Distribution Limitation Statement No. 2)

Short-term anneal experiments have been conducted on silicon and germanium bulk samples and on n-on-p and p-on-n silicon solar cells. Both conductivity and minority-carrier-lifetime measurements were made. All samples showed a reverse anneal in conductivity, i.e., an apparent continuation of radiation damage, following a neutron pulse. All materials showed a forward annealing of recombination lifetime, following the neutron pulse, which is enhanced by carrier injection. Annealing is stronger in p-type silicon than in n-type with more annealing occurring in higher resistivity n-type material than in low. This impurity concentration dependence is not evident in p-type material. Preparations are reported for further anneal experiments using an Accelerator Pulsed Fast Assembly (APFA) as a neutron source and recommendations are made as to the direction future investigations should pursue.

This page intentionally left blank.

CONTENTS

I. INTRODUCTION 1

II. BACKGROUND 2

III. THEORY 3
- 1. Short-term Annealing 3
- 2. Conductivity 5
- 3. Bulk Photoconductivity 6
- 4. Solar-cell Photoconductivity 6

IV. EXPERIMENT FACILITIES AND TECHNIQUES 11
- 1. TRIGA Mark I Experiments 11
- 2. ATPR Experiments 16
  - J-Tube 18
  - Void Tank 22
- 3. APFA III Experiments 28
- 4. Samples 40

V. EXPERIMENTAL RESULTS 41
- 1. Conductivity Samples 41
- 2. Bulk Photoconductivity Samples 41
- 3. Silicon Solar Cells 43

VI. DISCUSSION AND SUMMARY 62

VII. RECOMMENDATIONS FOR FUTURE INVESTIGATIONS 66

Appendix—DISCUSSION OF THE ANNEALING FACTOR 69

REFERENCES 74

FIGURES

1 Diagrammatic representation of a solar cell 7

2 Sample chamber (made of Fe for Ge and of Al for Si) used in TRIGA Mark I tests 15

3 Typical transient-power shape 17

4 J-tube position relative to reactor core, ATPR 19

5 J-tube position in core 20

6 Circuit used for monitoring short-term anneal conductivity samples 21

7 Typical oscillograph data from a 10-ohm-cm, p-type silicon conductivity sample 23

8 Void-tank cutaway view 25

9 Void-tank position relative to reactor core 26

10 Tank arrangement for ATPR with reactor in position for a void-tank experiment 27

11 Schematic of bulk-photoconductivity-sample test circuit 29

12 Schematic of silicon-solar-cell test circuit 29

FIGURES--continued

13 Typical solar-cell oscillograph record for a 10-ohm-cm p-base cell 30
14 Sketch of APFA assembly 32
15 Disassembled view of APFA III 33
16 N(E) dE vs E for GODIVA-type reactor (bare critical assembly) . . 34
17 APFA burst shape and Linac beam pulse for prompt multiplication of 250 36
18 Test circuit for APFA tests 37
19 Gate circuit for APFA tests 38
20 Noise signal in solar-cell test circuit for APFA experiments 38
21 Experiment configuration for APFA tests 39
22 Change in conductivity vs time for bulk-semiconductor samples following exposure to ~ 4.5 x 10^{13} nvt pulses in the J-tube of the ATPR facility 42
23 Time dependence of the ratio of radiation-induced to initial recombination center concentration in germanium bulk photoconductivity samples following a 2 x 10^{12} n/cm^2 pulse 44
24 Annealing factor vs time for two germanium bulk photoconductivity samples 45
25 Time dependence of the ratio of radiation-induced to initial recombination center concentration in a 50-ohm-cm, n-type silicon bulk photoconductivity sample following a 2 x 10^{12} n/cm^2 pulse 46
26 Annealing factor vs time for a 50-ohm-cm, phosphorus-doped, quartz-crucible-grown, n-type silicon bulk photoconductivity sample 47
27 Time dependence of the ratio of radiation-induced to initial recombination center concentration following a 2 x 10^{12} n/cm^2 pulse for phosphorus-doped, quartz-crucible-grown, p-on-n solar cells 48
28 Annealing factor vs time for two phosphorus-doped, quartz-crucible grown, p-on-n solar cells 49
29 Time dependence of the ratio of radiation-induced to initial recombination center concentration following a 2 x 10^{12} n/cm^2 pulse for arsenic-doped, quartz-crucible-grown, p-on-n solar cells 50
30 Annealing factor vs time for three arsenic-doped, quartz-crucible grown, p-on-n solar cells 51
31 Time dependence of the annealing factor for a 10-ohm-cm, arsenic-doped, quartz-crucible-grown, p-on-n solar cell following a 2 x 10^{12} n/cm^2 pulse 52
32 Time dependence of the ratio of radiation-induced to initial recombination center concentration following a 2 x 10^{12} 2 x 10^{12} n/cm^2 pulse 54

33	Time dependence of the ratio of radiation-induced to initial recombination center concentration following a 2×10^{12} n/cm^2 pulse for some 10-ohm-cm n-on-p solar cells	55
34	Time dependence of the annealing factor for boron-doped, quartz-crucible-grown, n-on-p solar cells following a 2×10^{12} n/cm^2 pulse	56
35	Time dependence of the annealing factor for aluminum-doped, Lopex-grown, n-on-p solar cells following a 2×10^{12} n/cm^2 pulse	57
36	Time dependence of the ratio of radiation-induced to initial recombination center concentration of two 10-ohm-cm, boron-doped, n-on-p solar cells following a 2×10^{12} n/cm^2 pulse, showing the effect on annealing of injection level	58
37	Time dependence of the annealing factor for two 10-ohm-cm, boron-doped, n-on-p solar cells, showing dependence of annealing on injection level	59
38	Solar-cell output with no light on during Linac pulse into unassembled APFA sphere	61
39	β vs t for two hypothetical transistors, A and B, following a neutron pulse of fluence Φ	71
40	$1/\beta$ vs Φ for two hypothetical transistors, A and B, with the fluence delivered in a low neutron flux	71
41	β vs t for two hypothetical transistors, C and D, following a neutron pulse of fluence Φ_0	72
42	$1/\beta$ vs Φ for two hypothetical transistors, C and D, with the fluence delivered in a low neutron flux	72

TABLES

I	TRIGA Mark I Reactor Performance for 250-kw Steady-state and 800-Mw Pulsing Operation	12
II	Advanced TRIGA Prototype Reactor Performance for 1-Mw Steady-state and 2000-Mw Pulsing Operation	13
III	APFA III Performance Characteristics for a Maximum Burst	14
IV	Spectrum Encountered at Sample Location in the J-tube	22
V	Spectrum in Void Tank with 1/4-in. Boral, 2-in. Lead, 1/4-in. Borated Plastic at Position No. 3 and 5-cm Water between Core Edge and Void Tank	24
VI	Solar-Cell Annealing Factors	53

This page intentionally left blank.

SECTION I
INTRODUCTION

The primary objectives of this study are to determine the nature and extent of short-term annealing of fission-neutron-induced damage effects in semiconductor materials and devices and to attempt to formulate a model that will explain the observed phenomena and will enable a prediction to be made of the effects of this annealing on other semiconductor devices.

In the experimental phase of the program, three General Atomic radiation facilities--TRIGA Mark I and TRIGA Mark F nuclear reactors and the Accelerator Pulsed Fast Assembly (APFA III)--were used. The reactors provide higher fluences than are available in the APFA III facility and are quite adequate for studying phenomena from about 10 msec and longer. The APFA III, while restricting experiments to those that can be performed with relatively low neutron fluence, theoretically enables resolution of the annealing data on a microsecond time scale. At this time, the APFA is the only laboratory radiation source capable of yielding data on this time scale.

SECTION II
BACKGROUND

Permanent damage to semiconductor devices due to irradiation in a high-energy neutron spectrum has been recognized as a mechanism of circuit and system degradation since the early days of radiation effects research. Defects are introduced by elastic collisions of neutrons with individual atoms and the subsequent passage of the recoil atoms through the lattice. The resulting defects appreciably alter the electrical characteristics of the materials such that the circuit semiconductor parts no longer behave electrically as designed and circuit performance is degraded or destroyed.

As the state of the art improved and as piece parts that would operate at very high frequencies were produced, the transient signals induced by a short pulse of gamma radiation were recognized as a second mechanism of circuit failure. Energy deposition in the form of ionization created current pulses within the circuits which could cause devices to malfunction or even fail through catastrophic burnout. Investigations of this mechanism required high-speed monitor and data-recording systems in order to observe the transient responses of the devices and circuit being considered.

As instrumentation became more sophisticated and investigations of material and device response to radiation pulses continued, new phenomena were observed. The first of these was high-energy neutron-induced ionization in semiconductor materials. Further investigation revealed a second phenomenon, which is now commonly known as short-term annealing. For short (< 10 msec) pulses of neutrons in which a high fluence is delivered in a short time, the electrical parameters of semiconductor devices exposed to this pulse are initially degraded to a much greater extent than observed for devices exposed to the same fluence delivered over longer time periods. However, this additional degradation was observed to decrease or "anneal out" over time scales of the order of tens or hundreds of milliseconds. A study of this short-term anneal phenomenon was the objective of this program.

SECTION III
THEORY

1. SHORT-TERM ANNEALING

The permanent damage to semiconductors as a result of neutron irradiation is caused by the displacement collisions of the recoiling primary and secondary atoms with other atoms of the crystal lattice. The damage factor, D, is proportional to the total neutron cross section, σ, and the amount of the primary atom recoil energy that is ultimately lost in displacement collisions. Hence,

$$D = f\sigma\bar{E}_r \tag{1}$$

where $\bar{E}_r$ is the average recoil energy of the primary atom and f is the fraction of this energy that is lost in displacement collisions. The factor f is given by the theory presented in Reference 1 and the average recoil energy is given by

$$\bar{E}_r = \frac{4A\bar{g}E_n}{(A+1)^2} \tag{2}$$

where A is the atomic mass of the recoil atom, E_n is the neutron energy, and g is a factor that allows for anisotropic elastic scattering and inelastic scattering events (Reference 2).

The rate of generation of displaced atoms can be calculated by multiplying the known flux at a given time by D, the damage factor, which is a function of neutron energy. If we consider D = 1 at a neutron energy of 1 Mev, the damage can then be considered as equivalent to that due to a fluence of monoenergetic 1-Mev neutrons.

Following the introduction of primary radiation-induced displacement damage, as discussed above, comes the formation of "secondary" defect centers, which is caused by the migration of primary defects. Of course, with this migration some of the simple vacancy-interstitial pairs

(Frenkel defects) recombine; however, many of these initial defects combine with each other or with lattice impurities to form stable complex configurations. Some of the simpler of these complexes are the Si-B1 (vacancy-oxygen) center (References 3 and 4) and the Si-G7 (divacancy) center (References 5 and 6). Each of these defect complexes has associated with it a number of possible energy states for the electrons that lie in the forbidden gap. It cannot be said a priori whether these centers will be more effective or less effective than the initial damage centers in removing carriers from the conduction mechanism or whether they will be more or less effective as recombination centers. Thus, the conductivity might recover somewhat from its value immediately after the exposure or, conversely, it might decrease even farther on formation of the secondary defects. Similarly, the minority-carrier lifetime might either increase or decrease from its value immediately following exposure. In the experiments reported here, the conductivity was observed to decrease and the minority-carrier lifetime to increase following irradiation.

The fact that this short-term annealing is observed in neutron-irradiated materials and not in electron-irradiation samples indicates that the phenomenon is associated with the type of damage peculiar to neutron irradiation. It has been postulated (Reference 7) that a localized cluster of lattice defects may be produced by a recoil from a single collision between an energetic neutron and an atom in the lattice. And, indeed, these damage clusters have been observed in electron microscope work on neutron-irradiated germanium (Reference8). Although there is not this direct evidence of clustering in silicon, there are several indirect indications that neutron irradiation results in damage clusters in silicon also. These arguments are summarized in a paper by Sander and Gregory (Reference 9). It is likely that early changes in silicon-device parameters are due to initial reordering processes within the cluster regions themselves, leading to the formation of defect complexes, such as divacancy, trivacancy, vacancy-oxygen, and vacancy-phosphorus, which are stable at

room temperature. Continued changes at later times are possibly due to migration of some of the defects out of the parent cluster and eventual formation of a stable complex. This might be associated, in part, with interstitial motion, for many interstitials will channel out of the vicinity of their parent cluster during the cluster formation (References 10 and 11).

However, it has been reported (Reference 12) that lifetime degradation with neutron irradiation is apparently not dependent on oxygen content or, in n-type silicon, on the amount or type of impurity, and in p-type silicon, it is only weakly dependent on the impurity. This lack of dependence on impurity concentration or type leads to the surmise that the lifetime degradation may be the result of a center associated with the cluster itself, which changes character as the makeup of defects within the cluster alters owing to secondary defect formation. Gossick (Reference 13) has discussed the cluster in terms of a potential well surrounding the cluster region which might well serve as the dominant recombination center. Then, as reordering takes place within the cluster, the size of the cluster or, at any rate, the range of its effectiveness, would change and thus alter the lifetime.

Three different sets of experiments were performed to study short-term annealing. One set of experiments involved the measurement of the permanent conductivity changes versus time in p- and n-type silicon and germanium. Another was to determine the change in recombination lifetime, τ, in n- and p-type silicon and germanium by measuring the photoconductivity induced by an external light source as a function of time following a neutron pulse. The third set of experiments was also designed to monitor changes in recombination lifetime, but the parameter measured was the short-circuit current output of p-on-n and n-on-p silicon solar cells.

2. CONDUCTIVITY

As a result of defects caused by irradiation, additional energy levels are introduced within the forbidden band. These additional levels provide sites which remove electrons from the conduction mechanism and result in conductivity changes. As the mobility at room temperature is

governed primarily by lattice interactions for materials with low impurity concentrations, such as those used in these studies, the mobility is not greatly affected by the radiation, and changes in conductivity in these extrinsic samples are directly proportional to changes in carrier concentration, i.e.,

$$\frac{\Delta\sigma}{\sigma_0} \simeq \frac{\Delta n}{n_0} \tag{3}$$

where σ_0 = initial conductivity,

$\Delta\sigma$ = radiation-induced conductivity change,

n_0 = initial carrier concentration,

Δn = radiation-induced changes in carrier concentration.

Thus, plots of $\Delta\sigma/\sigma_0$ for the conductivity samples are in fact plots of the fractional change in carrier concentration, $\Delta n/n_0$.

3. BULK PHOTOCONDUCTIVITY

Measurement of the photoconductivity developed in n- and p-type silicon and germanium semiconductor samples by a constant light source was used to determine the minority-carrier lifetime in the samples from the relation

$$\Delta\sigma = g\tau e(\mu_n + \mu_p) \tag{4}$$

Here, $\Delta\sigma$ is the conductivity increase caused by the light, g is the carrier generation rate due to the light, τ is the recombination rate, or minority-carrier lifetime (thus, $g\tau$ is the equilibrium number of additional electron-hole pairs present when the sample is illuminated), e is the electron charge, and μ_n and μ_p are the mobilities of the electrons and holes, respectively.

4. SOLAR-CELL PHOTOCONDUCTIVITY

The third experiment involved measuring the short-circuit photocurrent from both n-on-p and p-on-n silicon solar cells, and from these measurements, the lifetime of minority carriers in the base material could be deduced. Thus, these experiments were an attempt to observe the short-term annealing of minority-carrier lifetime, as were the bulk photoconductivity experiments.

The dependence of the short-circuit photocurrent on the lifetime in the base material may be seen in the following analysis, in which, for explicitness, the discussion is confined to a p-on-n cell (see Figure 1).

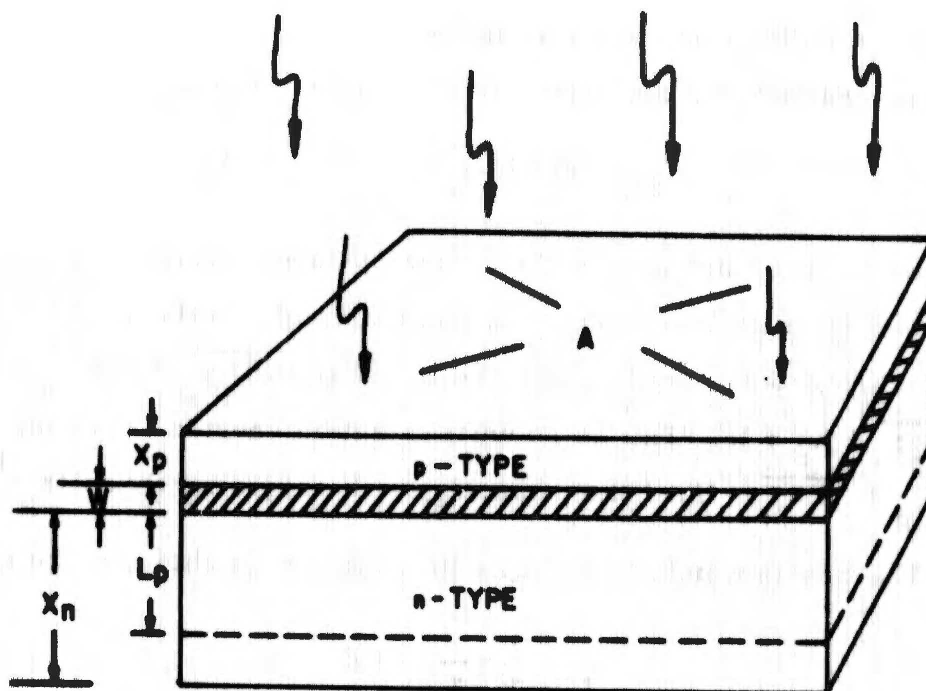

Figure 1. Diagrammatic representation of a solar cell

The same analysis, with a change in subscripts, holds equally well for an n-on-p cell:

$$I_{SC} = geA(L_p + L_n + W) \tag{5}$$

where I_{SC} = short-circuit photocurrent,

g = generation rate of electron-hole pairs in material by light (assumed in this simplified analysis to be constant throughout the material),

e = electronic charge,

A = area of the junction,

L_p = diffusion length of holes in the n region,

L_n = diffusion length of electrons in the p region,

W = width of the junction depletion layer.

Since the diffusion length and minority-carrier lifetime are related by

$$L = \sqrt{D\tau} \quad (6)$$

where D is the diffusion constant for the minority carrier in a given material, the equation for the short-circuit current may be rewritten as

$$I_{SC} = geA(\sqrt{D_p\tau_p} + \sqrt{D_n\tau_n} + W) \quad (7)$$

Furthermore, the thickness of the surface p-layer diffusion, X_p, in a normal cell is much less than L_n in this material, so the actual volume from which carriers may be collected is not $geA(\sqrt{D_p\tau_p} + \sqrt{D_n\tau_n} + W)$ but $geA(\sqrt{D_p\tau_p} + X_p + W)$. This is so until radiation shortens τ_n to the point where $X_p > \sqrt{D_n\tau_n}$. Until this time, I_{SC} will vary directly as $(\tau_p)^{1/2}$.

The way in which τ changes with radiation is shown in the equation

$$\frac{1}{\tau} = \frac{1}{\tau_0} + K\Phi \quad (8)$$

where τ is the post-irradiation lifetime, τ_0 is the initial lifetime, K is an empirical constant, and Φ is the total neutron fluence.

Typical surface-layer diffusions are of the order of 0.5 μ and $D_n \approx 35\ cm^2/sec$. Using the empirically determined value of K for p-type silicon and assuming that τ_0 is large enough that $1/\tau_0$ may be neglected, we may then calculate to what level of fluence this square-root dependence can be expected to hold. It will cease to hold at the point where

$$X_p = \sqrt{D_n\tau_n} \quad (9)$$

but

$$\frac{1}{\tau_n} \approx K\Phi \quad (10)$$

so this is the point where

$$X_p = \sqrt{D_n/K\Phi} \quad (11)$$

or where

$$\Phi = \frac{D_n}{KX_p^2} \tag{12}$$

Substituting the above values, we obtain

$$\Phi = \frac{35\ \text{cm}^2/\text{sec}}{2 \times 10^{-7}\ \text{cm}^2/\text{neutron-sec} \times 25 \times 10^{-10}\ \text{cm}^2} \tag{13}$$

or

$$\Phi = 7 \times 10^{18}\ \text{neutrons/cm}^2 \tag{14}$$

Therefore, for irradiation fluences encountered in these tests, the requirement for a square-root dependence of the short-circuit current on end-point minority-carrier lifetime was easily met.

Equation (7), the equation for short-circuit current as a function of minority-carrier lifetime, may be rewritten as

$$I_{SC} = C_1 + C_2\tau_p^{1/2} \tag{15}$$

where $C_1 = geA(X_p + W)$,

$C_2 = geAD_p^{1/2}$.

Since $C_1 << C_2\tau_p^{1/2}$ for all reasonable values of τ_p,

$$\tau_p \approx C_3 I_{SC}^2 , \tag{16}$$

where $C_3 = 1/C_2^2$. Therefore, a function, R, may be defined as

$$R = \frac{1/I^2 - 1/I_0^2}{1/I_0^2} = (I_0/I)^2 - 1 \tag{17}$$

or as

$$R = \frac{1/\tau - 1/\tau_0}{1/\tau_0} = (\tau_0/\tau) - 1 \tag{18}$$

i.e., the fractional change in the square of the reciprocal short-circuit current (the subscript SC has been dropped for convenience) is equal to the fractional change in reciprocal lifetime.

As the change in reciprocal lifetime is proportional to irradiation fluence and thus to the number of radiation-induced recombination centers, a plot of the function R versus time is a plot of the ratio of the number of radiation-induced recombination centers to the number present before irradiation. This plot clearly shows the annealing of the radiation-induced centers.

SECTION IV
EXPERIMENT FACILITIES AND TECHNIQUES

Three General Atomic neutron-irradiation facilities were used in these experiments: TRIGA Mark I reactor was used for preliminary checks on sample chambers to be used in the conductivity anneal tests; the Advanced TRIGA Prototype Reactor (ATPR) was used for the majority of the conductivity and lifetime anneal experiments reported here; and the Accelerator Pulsed Fast Assembly (APFA) was used to extend these measurements into the very short time (microseconds) domain in which data is unobtainable using other facilities. Tables I, II, and III list the pertinent characteristics of the three facilities.

1. TRIGA MARK I EXPERIMENTS

One of the problems associated with studying short-term annealing following a high-neutron-flux pulse is the separation of effects due to temperature changes and those due to annealing. Associated with high-fluence neutron pulses is a pulse of high-energy gamma radiation. This gamma contribution, which is absorbed in the sample and sample chamber, causes a temperature rise proportional to the square of the atomic number (Z). If the sample chamber is constructed of a material which has a Z widely different from that of the sample, the temperature reached by the sample initially will be quite different from that of the chamber. Since the chamber is much more massive than the sample, the sample then equilibrates to the chamber temperature, with consequent changes in sample properties. However, if the sample chamber is constructed of material with a Z very close to that of the sample, both will reach the same temperature caused by the gamma flux and the thermal relaxation will then be that of the unit. This greatly simplifies the separation of temperature effects because it is relatively simple to insulate the sample chamber from its surroundings well enough to effect thermal-relaxation time constants of tens of seconds,

TABLE I

TRIGA MARK I REACTOR PERFORMANCE

FOR 250 kw STEADY-STATE AND 1000-Mw PULSING OPERATION

(Experimental dosimetry values for a typical core loading of 70 fuel elements)

Experimental Location	Volume With < 10% Flux Variation	250 kw Steady State Operation			1000-Mw Pulsing Operation[a]						
		Neutrons, nv			Peak Dose Rate			Dose Per Pulse			
					Neutrons, nv			Neutrons			
		Fast (> 10 kev)	Thermal (< 0.4 ev)	Gammas (rads/sec)	Fast (> 10 kev)	Thermal (< 0.4 ev)	Gammas (rads/sec)	Fast (nvt)	Fast (rads[e])	Thermal (nvt[f])	Gammas (rads)
B ring[b]	1.25-in. dia x 6 in.	1.4×10^{13}	4.5×10^{12}	-	5.4×10^{16}	1.8×10^{16}	-	9.7×10^{14}	2.4×10^{6}	3.2×10^{14}	-
C ring[b]	1.25-in. dia x 6 in.	1.2×10^{13}	6.3×10^{12}	-	4.9×10^{16}	2.5×10^{16}	-	8.8×10^{14}	2.2×10^{6}	4.5×10^{14}	-
D ring[b]	1.25-in. dia x 6 in.	1.1×10^{13}	5.3×10^{12}	4.2×10^{4}	4.2×10^{16}	2.1×10^{16}	1.7×10^{8}	7.6×10^{14}	1.9×10^{6}	3.8×10^{14}	3.0×10^{6}
E ring[b]	1.25-in. dia x 6 in.	8.0×10^{12}	4.3×10^{12}	-	3.2×10^{16}	1.7×10^{16}	-	5.8×10^{14}	1.5×10^{6}	3.0×10^{14}	-
F ring[b]	1.25-in. dia x 6 in.	5.3×10^{12}	2.5×10^{12}	1.5×10^{4}	2.1×10^{16}	1.0×10^{16}	6.1×10^{7}	3.8×10^{14}	9.5×10^{5}	1.8×10^{14}	1.1×10^{6}
Pneumatic transfer system terminus in F ring	0.5-in. dia x 3.8-in. long (in specimen capsule	5.3×10^{12}	2.5×10^{12}	1.5×10^{4}	2.1×10^{16}	1.0×10^{16}	6.1×10^{7}	3.8×10^{14}	9.5×10^{5}	1.8×10^{14}	1.1×10^{6}
Rotary specimen rack	40 containers (0.8-in. ID x 3.8-in. each)	1.5×10^{12}	1.8×10^{12}	4.0×10^{3}	6.0×10^{15}	7.2×10^{15}	1.6×10^{7}	1.1×10^{14}	2.7×10^{5}	1.3×10^{14}	2.9×10^{5}
Reactor pool outside reflector	c	1.7×10^{10}	6.6×10^{11}	4.0×10^{2}	6.8×10^{13}	2.6×10^{15}	1.6×10^{6}	1.2×10^{12}	3.0×10^{3}	4.7×10^{13}	2.8×10^{4}
Reactor pool above top of reflector	d	1.1×10^{11}	3.4×10^{11}	-	4.4×10^{14}	1.5×10^{15}	-	7.9×10^{12}	2.0×10^{4}	2.5×10^{13}	-

[a] Insertion of 2.2% δk/k excess reactivity ($3.00) results in a peak power of 1000 Mw, a total integrated energy release of 18 Mw-sec, and a pulse width of 16.6 msec.

[b] A varying number of fuel element positions in the core grid array may be occupied by experiments.

[c] Volume available has 1.7-foot inside radius and 3-foot outside radius. Flux decreases by inverse square law attenuation with distance from reflector

[d] Specimen with a diameter of 1 foot or less placed on top of the reflector will receive a fairly uniform flux.

[e] Fast neutron dose is converted from nvt to rads by multiplying the nvt value by 2.5×10^{-9} rads/n-cm^2.

[f] Thermal neutron dose is converted from nvt to rads by multiplying the nvt value by 3.25×10^{-10} rads/n-cm^2.

TABLE II

ADVANCED TRIGA PROTOTYPE REACTOR PERFORMANCE FOR 1.5-Mw STEADY-STATE AND 6400-Mw PULSING OPERATION
(Experimental dosimetry values for a typical core loading of 94 fuel elements)

Experimental Location	Volume With < 10% Flux Variation	1.5-Mw Steady-State Operation			6400-Mw Pulsing Operation[a]						
					Peak Dose Rate			Dose Per Pulse			
		Neutrons, nv			Neutrons, nv			Neutrons			
		Fast (> 10 kev)	Thermal (< 0.4 ev)	Gammas (rads/sec)	Fast (> 10 kev)	Thermal (< 0.4 ev)	Gammas (rads/sec)	Fast, nvt (> 10 kev)	Fast rads[f]	Thermal, nvt[g] (< 0.4 ev)	Gammas (rads)
B ring[b]	1.25-in. dia x 6 in.	3.3×10^{13}	4.4×10^{13}	9.9×10^{4}	1.4×10^{17}	1.9×10^{17}	4.2×10^{8}	9.5×10^{14}	2.4×10^{6}	1.2×10^{15}	2.8×10^{6}
C ring[b]	1.25-in. dia x 6 in.	3.2×10^{13}	3.5×10^{13}	8.3×10^{4}	1.3×10^{17}	1.5×10^{17}	3.5×10^{8}	9.0×10^{14}	2.2×10^{6}	9.9×10^{14}	2.4×10^{6}
D ring[b]	1.25-in. dia x 6 in.	2.8×10^{13}	3.0×10^{13}	6.6×10^{4}	1.2×10^{17}	1.3×10^{17}	2.8×10^{8}	7.7×10^{14}	1.9×10^{6}	8.6×10^{14}	1.9×10^{6}
E ring[b]	1.25-in. dia x 6 in.	2.0×10^{13}	2.7×10^{13}	5.0×10^{4}	8.3×10^{16}	1.1×10^{17}	2.1×10^{8}	5.6×10^{14}	1.4×10^{6}	7.3×10^{14}	1.4×10^{6}
F ring[b]	1.25-in. dia x 6 in.	1.2×10^{13}	2.3×10^{13}	3.3×10^{4}	5.2×10^{16}	9.6×10^{16}	1.4×10^{8}	3.5×10^{14}	8.8×10^{5}	6.5×10^{14}	9.5×10^{5}
G ring[b]	1.25-in. dia x 6 in.	6.6×10^{12}	2.4×10^{13}	2.1×10^{4}	2.8×10^{16}	1.0×10^{17}	9.0×10^{7}	1.9×10^{14}	4.8×10^{5}	6.9×10^{14}	6.0×10^{5}
J-tube	5-in. dia x 10 in.	4.5×10^{12}	2.4×10^{13}	2.1×10^{4}	1.9×10^{16}	1.0×10^{17}	9.0×10^{7}	1.3×10^{14}	3.3×10^{5}	6.9×10^{14}	6.0×10^{5}
Void tank:[c] Tube No. 1	4.25 in. dia x 10 in.	9.9×10^{11}	1.0×10^{11}	4.4×10^{3}	4.2×10^{15}	4.5×10^{14}	1.9×10^{7}	2.8×10^{13}	7.0×10^{4}	3.1×10^{12}	1.3×10^{5}
Tube No. 2	4.25 in. dia x 10 in.	3.5×10^{11}	----	1.8×10^{3}	1.5×10^{15}	-----	7.7×10^{6}	9.9×10^{12}	2.5×10^{4}	-----	5.2×10^{4}
Tube No. 3	4.25 in. dia x 10 in.	1.7×10^{11}	1.5×10^{11}	9.3×10^{2}	7.0×10^{14}	6.4×10^{14}	4.0×10^{5}	4.7×10^{12}	1.2×10^{4}	4.3×10^{12}	2.7×10^{4}
Tube No. 4	4.25 in. dia x 10 in.	9.3×10^{10}	----	6.0×10^{2}	4.0×10^{14}	-----	2.7×10^{5}	2.7×10^{12}	6.8×10^{3}	-----	1.7×10^{4}
Thermal column:[d] Tube No. 2 Gold R_{Cd} = 63	4.25 in. dia x 10 in.	1.7×10^{9}	2.[illegible] $\times 10^{11}$	2.1×10^{1}	7.0×10^{12}	9.6×10^{14}	8.8×10^{4}	4.7×10^{10}	1.2×10^{2}	6.5×10^{12}	5.9×10^{2}
Thermal column:[d] Tube No. 3 Gold R_{Cd} = 223	4.25 in. dia x 10 in.	2.0×10^{8}	6.3×10^{10}	4.9×10^{0}	8.3×10^{11}	2.7×10^{14}	2.1×10^{4}	5.6×10^{9}	1.4×10^{1}	1.8×10^{12}	1.4×10^{2}
Reactor pool, outside core shroud	e	4.2×10^{12}	1.5×10^{13}	1.3×10^{4}	1.8×10^{16}	6.4×10^{16}	5.6×10^{7}	1.2×10^{14}	3.0×10^{5}	4.3×10^{14}	3.7×10^{5}

[a] Insertion of 3.22% δk/k excess reactivity results in a peak power of 6400-Mw, a total integrated energy release of 43 Mw-sec, and a pulse width a half maximum of 6.3 msec.

[b] A varying number of fuel element positions in the core grid array may be occupied by experiments.

[c] Void tank is semicircular in shape, 35 inches high, and 46 inches in radius, therefore permitting easy irradiation of large experimental devices. Fluxes are given for the four experimental tubes with 1/4-inch boral shield plus 5 cm of water between core edge and tank.

[d] Fluxes are given for the thermal column with 5 cm of water between core edge and column.

[e] The annular volume between the core shroud and the pool tank (10-ft diameter) is available for bulk experiments. Fluxes are given for a position next to the shroud.

[f] Fast neutron dose is converted from nvt to rads by multiplying the nvt value by 2.5×10^{-9} rads/n-cm^2.

[g] Thermal neutron dose is converted from nvt to rads by multiplying the nvt value by 3.24×10^{-10} rads/n-cm^2.

Table III

APFA III PERFORMANCE CHARACTERISTICS FOR A MAXIMUM BURST

Characteristic	Value
Excess reactivity	\$0.86
Prompt multiplication	1000
Prompt α	$-1.5 \times 10^{+5}$ sec^{-1}
Fission rate	$\approx 1 \times 10^{20}$ fissions/sec
Pulse width 1/2 maximum	≈ 8 μsec
Fission yield	$\approx 1 \times 10^{15}$ fissions
Leakage rate	$\approx 1.5 \times 10^{20}$ neutrons/sec
Leakage neutrons	$\approx 1.5 \times 10^{15}$ neutrons
Total radiation at closest approach	$\approx$ 300 R gamma $\approx$ 2000 rem fast neutrons
Neutron fluence	$\approx 2-5 \times 10^{12}$ neutrons/cm^2

whereas it is difficult to attain this degree of isolation of the sample from the chamber. The sample chambers (see Figure 2) constructed on this theory were of iron (Z = 26) for use with germanium (Z = 32) samples and transistors in nickel (Z = 28) cans and were of aluminum (Z = 13) for silicon (Z = 14) samples.

When checked in tests in the TRIGA Mark I reactor, it was found that the temperature rise in both germanium and silicon bulk samples and their respective sample chambers was as predicted by the known gamma flux, and these samples then maintained this temperature for the full 10-sec measurement time. Evidently, sample chambers constructed in this way would enable short-term annealing experiments to be made which would be free of temperature effects. However, the tests of the iron transistor sample chamber with a 2N2222 transistor mounted in it yielded anomalous results. From dc current-gain (β) measurements during this test, from the transistor-case temperature recorded during the test, and from β

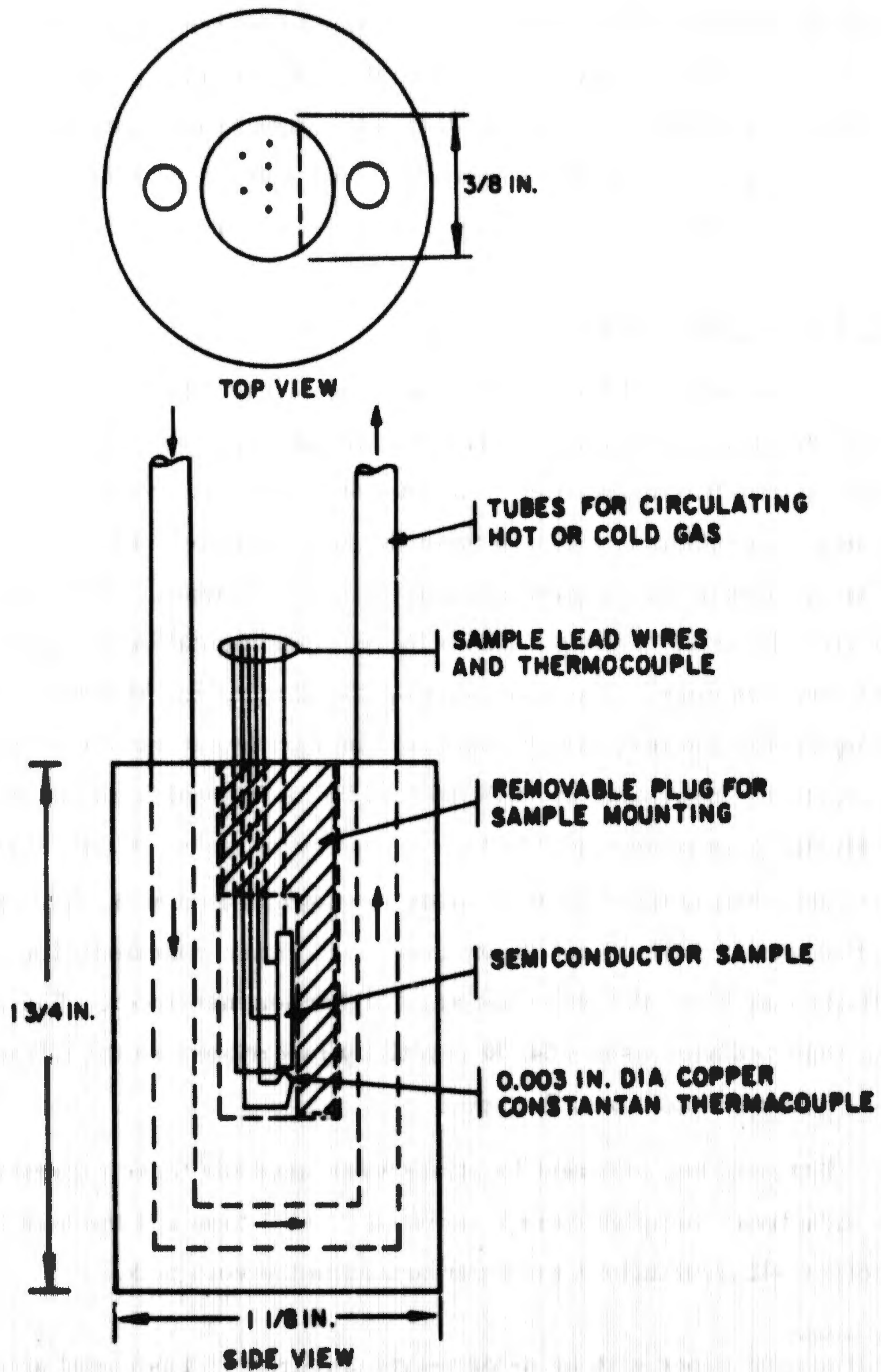

Figure 2. Sample chamber (made of Fe for Ge and of Al for Si) used in TRIGA Mark I tests

versus temperature measurements made in the laboratory, it was determined that the transistor-chip temperature exceeded the transistor-case temperature by about 10°C. Investigation into the manufacturing technique used in making this transistor revealed that the silicon chip is attached to the transistor header with a gold preform.* This gold (Z = 79) is believed to be the cause of the anomalous temperature rise in the chip.

2. ATPR EXPERIMENTS

The Advanced TRIGA Prototype Reactor (ATPR) is a semihomogeneous reactor utilizing a U-ZrH alloy for fuel and water for cooling and partial neutron thermalization. The fuel elements are rod type and are positioned in concentric rings to form the reactor core. The water-reflected core is suspended from a movable bridge in a 10-ft diam, 25-ft deep water-filled pit. The size of the pit allows large experimental devices to be placed near the core. The reactor is operated up to 1.5 Mw(th) in steady-state operation and may also be operated in a transient mode with routine step reactivity insertions up to $4.60 (3.22% $\Delta k/k$), which yields about 6400 Mw(th) peak power and 43 Mw-sec energy release. A typical transient power pulse during this transient mode is shown in Figure 3. This pulse was obtained for a $3.00 reactivity insertion. When operated with a higher reactivity insertion, the pulse becomes higher and narrower. The experiments reported here used ~$4.00 reactivity insertions, so the full width at half maximum was about 7 msec.

Either of two different locations were used for these experiments. The conductivity samples were irradiated in the J-tube and the bulk lifetime and solar-cell irradiations were performed in the void tank.

*A foil of gold doped with an n- or p-type impurity (< 1 percent) and containing about 1 percent silicon to facilitate the formation of the gold-silicon eutectic, which is alloyed to the transistor chip and the header to bond the two together.

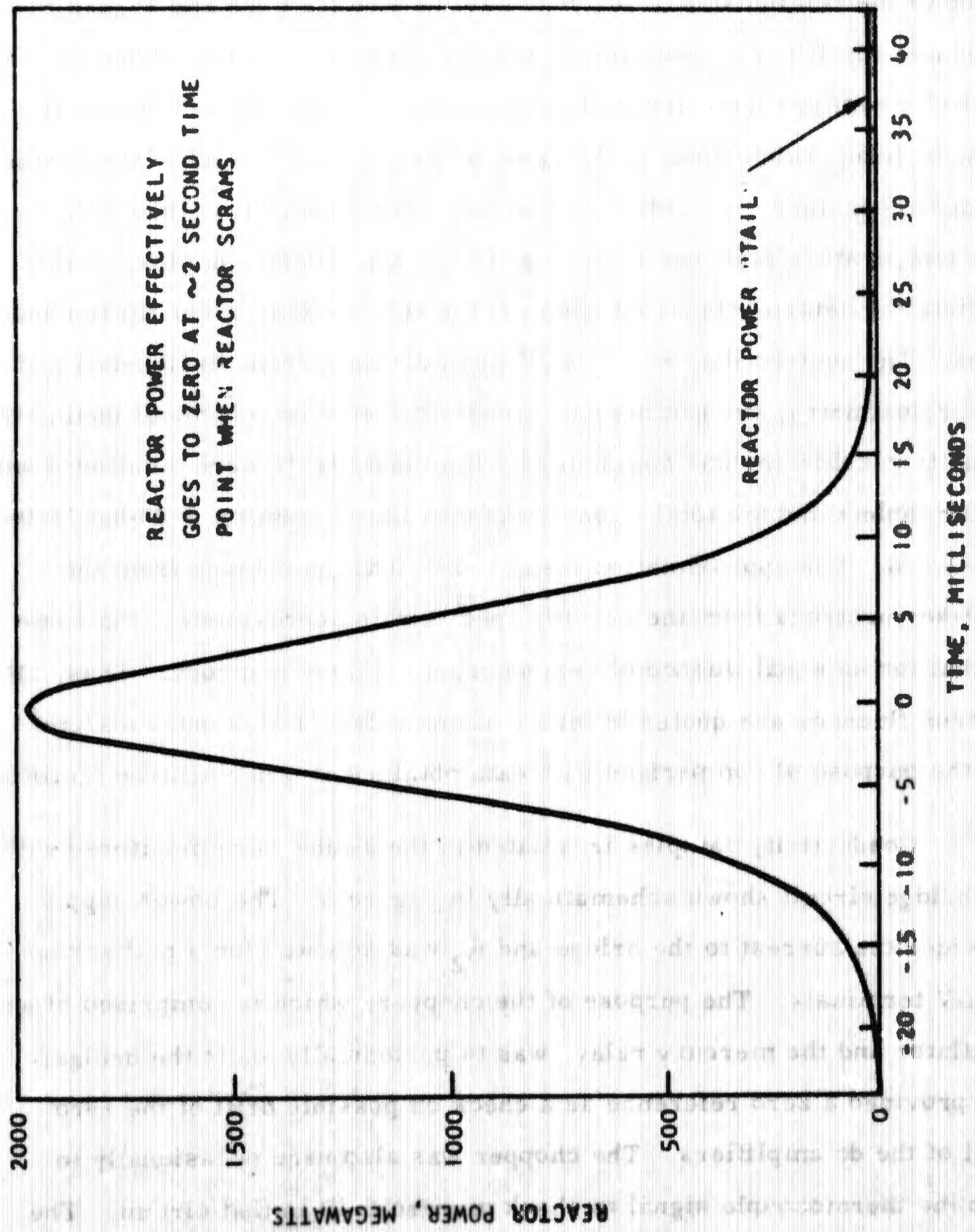

Figure 1. Typical transient-power shape

J-Tube

The J-tube is a 6-in.-ID tube that extends from the top of the reactor pit through the pit water to the edge of the reactor core. Figure 4 shows the relationship of the J-tube to the reactor core and Figure 5 indicates the J-tube irradiation volume in the reactor core. When the conductivity samples were irradiated in the J-tube, they were shielded with 2 in. of lead, which reduced the gamma dose to a level such that the maximum temperature rise in the germanium samples was less than 3°C. The temperature rise was even smaller for the silicon samples. Table IV lists the neutron spectrum encountered in the J-tube under these conditions. The neutron data in Table IV were obtained from fission-foil and sulfur dosimetry; the gamma data were obtained from chemical dosimetry using tetrachlorethylene dosimeters. Individual tests were monitored with sulfur tablets and the total fluence was calculated from the > 10-kev/3.0-Mev ratio. The approximation then used is that the damage from the > 10-kev neutrons from the reactor spectrum is approximately the same as that for an equal fluence of monoenergetic 1-Mev neutrons. Thus, all neutron fluences are quoted in terms of equivalent 1-Mev neutrons/cm^2 for the purpose of comparison with data obtained at other neutron facilities.

Conductivity samples irradiated in the J-tube were monitored with the bridge circuit shown schematically in Figure 6. The power supply provided the current to the bridge and R_2 was adjusted for a null across the ΔV terminals. The purpose of the chopper, which is comprised of an oscillator and the mercury relay, was to periodically short the bridge; this provided a zero reference as a check on possible drift of the zero level of the dc amplifiers. The chopper was also used occasionally to chop the thermocouple signal to check on zero drift in that circuit. The 400-ohm resistor across the dc power supply ensured that there would be no power-supply transients induced by the use of the chopper. Radiation-induced signals were recorded both on oscilloscopes and on the

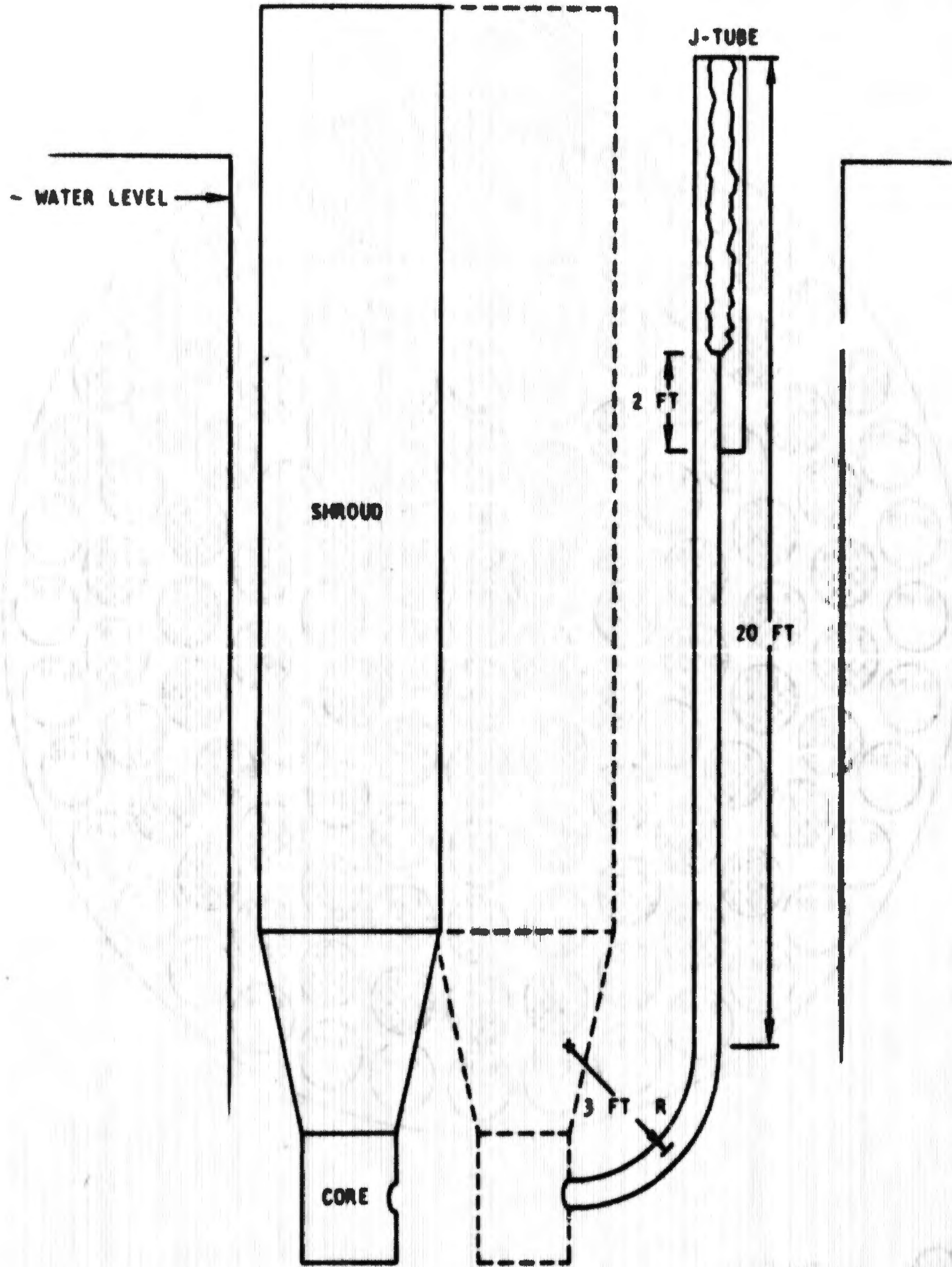

Figure 4. J-tube position relative to reactor core, ATPR

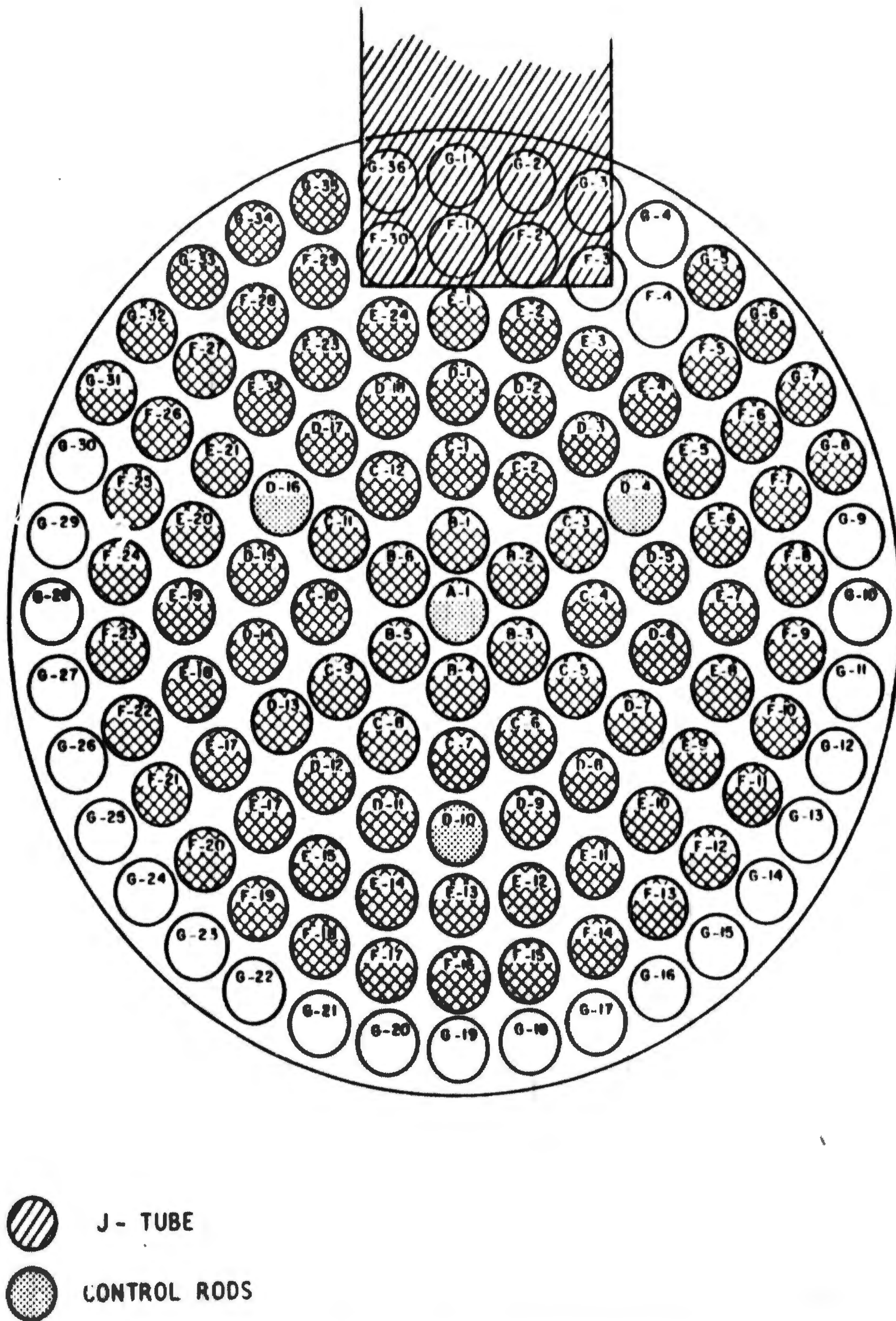

Figure 5. J-tube position in core

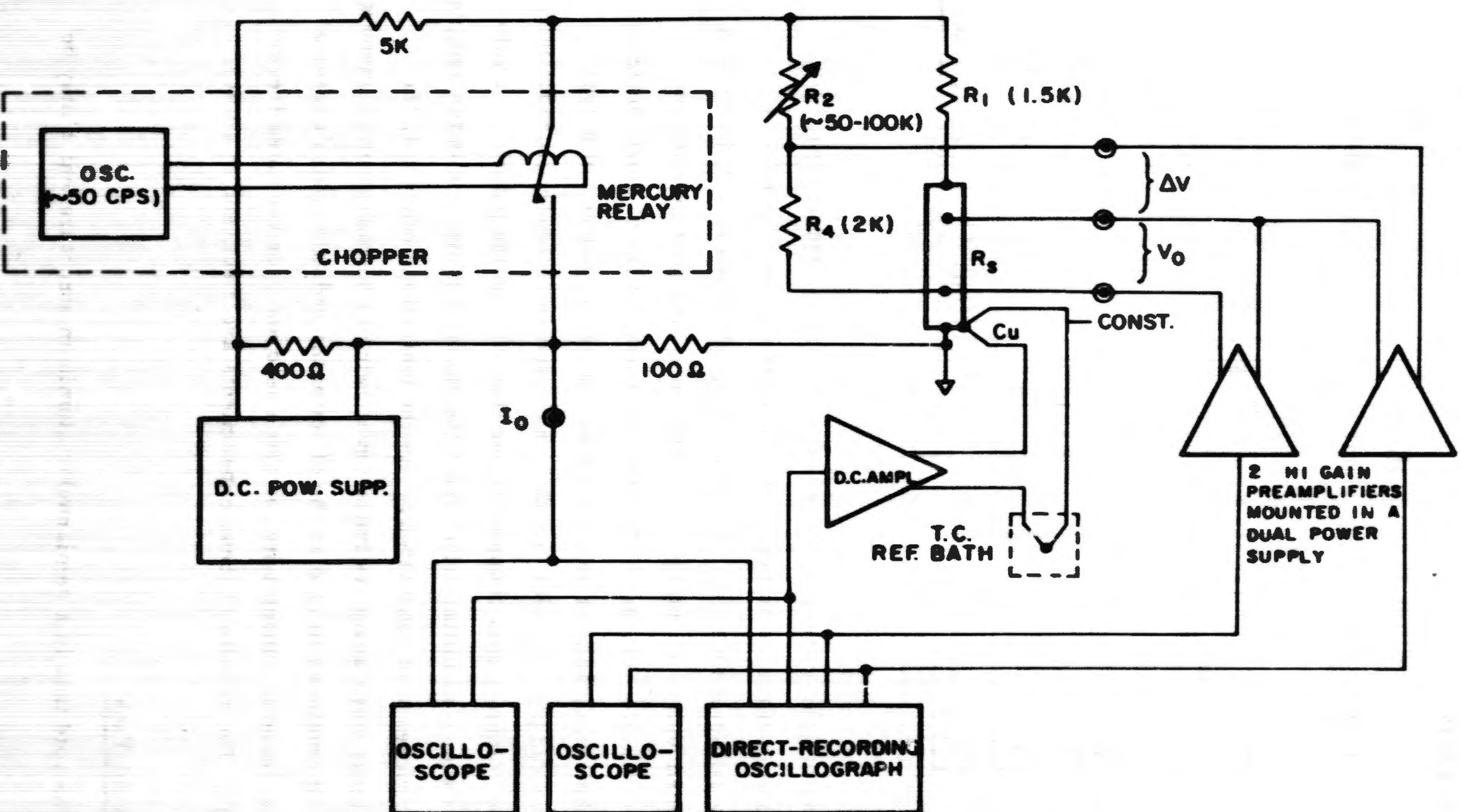

Figure 6. Circuit used for monitoring short-term anneal conductivity samples

Table IV

SPECTRUM ENCOUNTERED AT SAMPLE LOCATION IN THE J-TUBE*

J-tube ($\bar{\bar{E}}_n$ = 0.79 Mev)

Neutron Energy	nv/watt	Integrated Flux for 40-Mw-sec pulse, nvt	Flux for 4800-Mw pulse, nv
> 10 kev	1.2×10^6	4.6×10^{13}	5.4×10^{15}
> 0.6 Mev	6.5×10^5	2.6×10^{13}	3.1×10^{15}
> 1.5 Mev	3.8×10^5	1.5×10^{13}	1.9×10^{15}
> 3.0 Mev	7.7×10^4	3.1×10^{12}	3.7×10^{14}
Gamma	0.28 rads/sec/w	1.2×10^5 rads (Si)	1.3×10^7 rads

*Data for $4.00 reactivity insertion with 2-in. lead shield.

oscillograph in early tests; however, it was soon recognized that no additional data were contained in the oscilloscope photographs, so only the oscillograph was used in later tests. Portions of a typical oscillograph record with no chopping during the immediate post-irradiation period are shown in Figure 7. These traces are typical of those observed in all of the conductivity tests with the exception, of course, of p-type germanium samples in which irradiation caused an increase in conductivity so that the voltage signal dropped rather than rose at the pulse. The voltage trace shows an initial drop during the pulse as ionization in the sample causes an increase of conductivity. As the ionization decays out, the voltage signal rises above its initial level owing to permanent displacement damage. It continues to rise as the effect of the radiation pulse causes a further decrease in conductivity for some seconds after the pulse (reverse annealing). The results of these experiments are discussed in a later section.

Void Tank

The void tank is a semiannular aluminum structure which may be

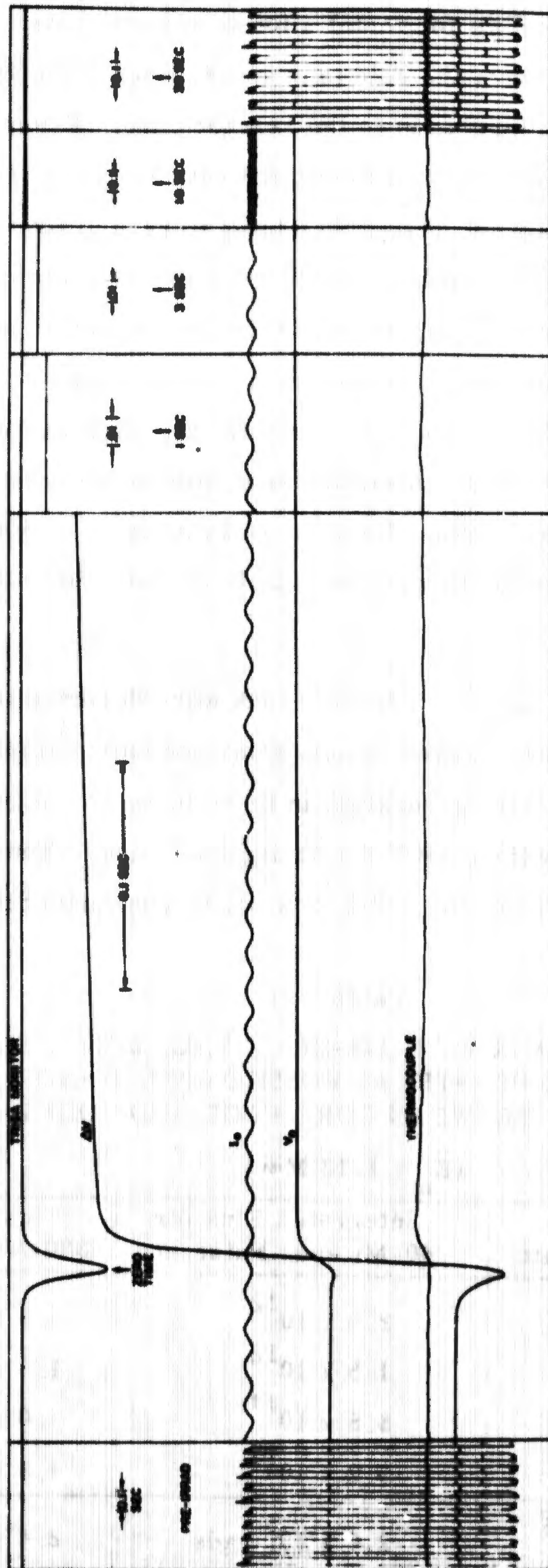

Figure 7. Typical oscillograph data from a 10-ohm-cm, p-type silicon conductivity sample

removed from the reactor pit for installation of shielding materials. Figure 8 is a cutaway view of the void tank and Figures 9 and 10 show the position of the void tank in relation to the reactor core. Experiments reported on here were conducted in Position 3 with 1/4 in. of boral, 2 in. of lead, and 1/4 in. of borated plastic shielding to reduce both thermal neutron flux and gamma dose at the samples. There is some additional shielding from the water (~ 5 cm) between the reactor shroud and the core itself. With this configuration, the spectrum to which the samples were exposed is given in Table V. The dosimetry for the void tank was performed as for the J-tube, with individual tests being monitored with sulfur-pellet dosimetry. As the gamma flux is down by a factor of 500 from that in the J-tube, temperature effects were negligible in tests conducted in the void tank.

Experiments conducted in the void tank were designed to monitor minority-carrier lifetime changes in bulk semiconductor samples and in silicon solar cells. Carrier generation in these tests was accomplished with a light source. A 625-w, 3400°K floodlight was used. The lamp was mounted at the end of a 24-ft long, 2-1/2-in.-diam aluminum tube and a

Table V

SPECTRUM IN VOID TANK WITH 1/4-IN. BORAL, 2-IN. LEAD, 1/4-IN. BORATED PLASTIC AT POSITION NO. 3 AND 5 CM WATER BETWEEN CORE EDGE AND VOID TANK

($\bar{E}_n$ = 1.12 Mev)

Neutron Energy	nv/watt	Integrated Flux for 40-Mw-sec Pulse, nvt	Flux for 4800-Mw Pulse, nv
> 10 keV	7.3×10^4	2.9×10^{12}	3.5×10^{14}
> 0.6 Mev	3.8×10^4	1.5×10^{12}	1.8×10^{14}
> 1.5 Mev	2.2×10^4	8.8×10^{11}	1.0×10^{14}
> 3.0 Mev	8.0×10^3	3.2×10^{11}	3.8×10^{13}
Gamma	5.0×10^{-5} rads/sec/w	2.0×10^3 rads	2.4×10^5 rads sec

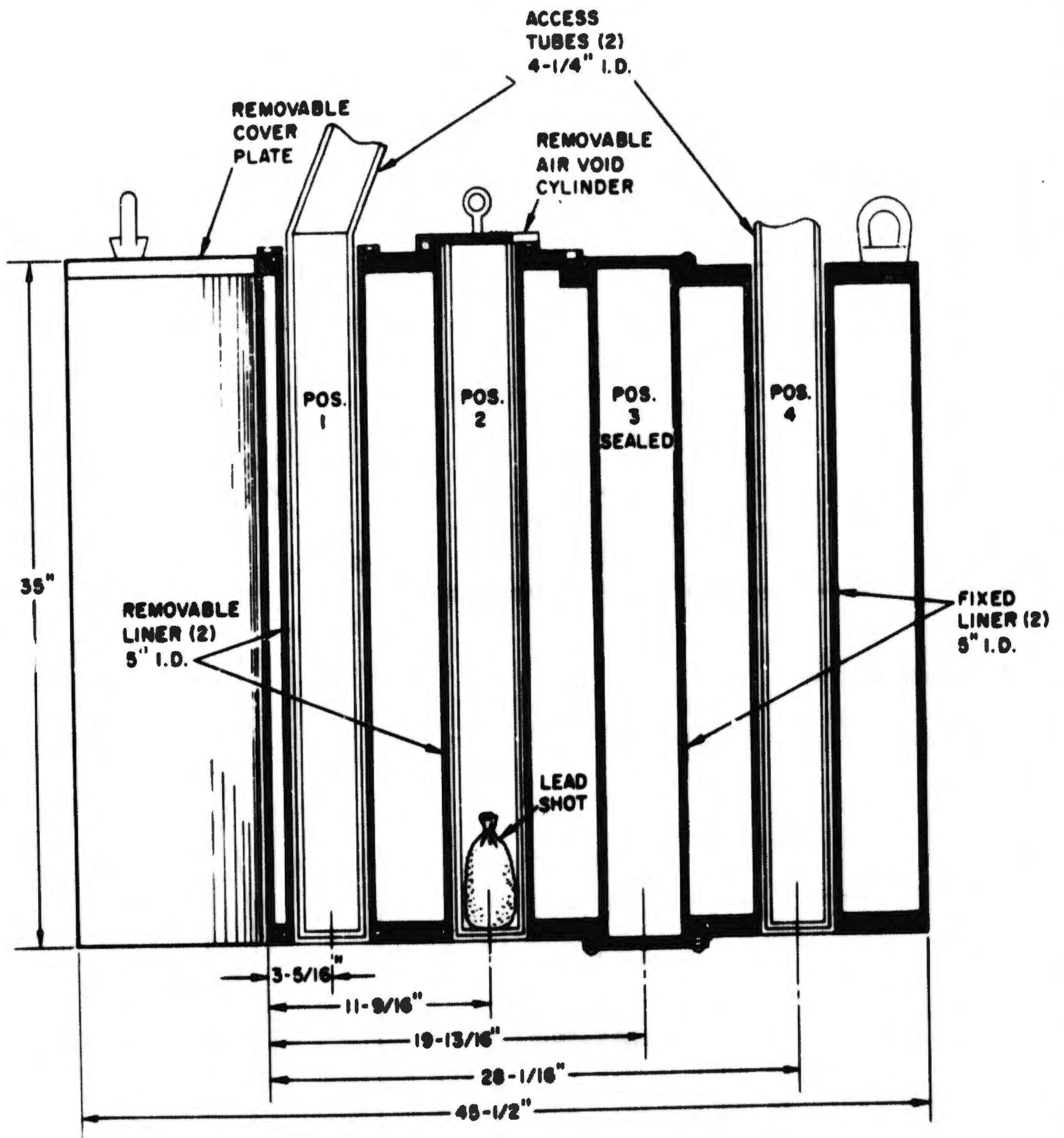

Figure 8. Void-tank cutaway view

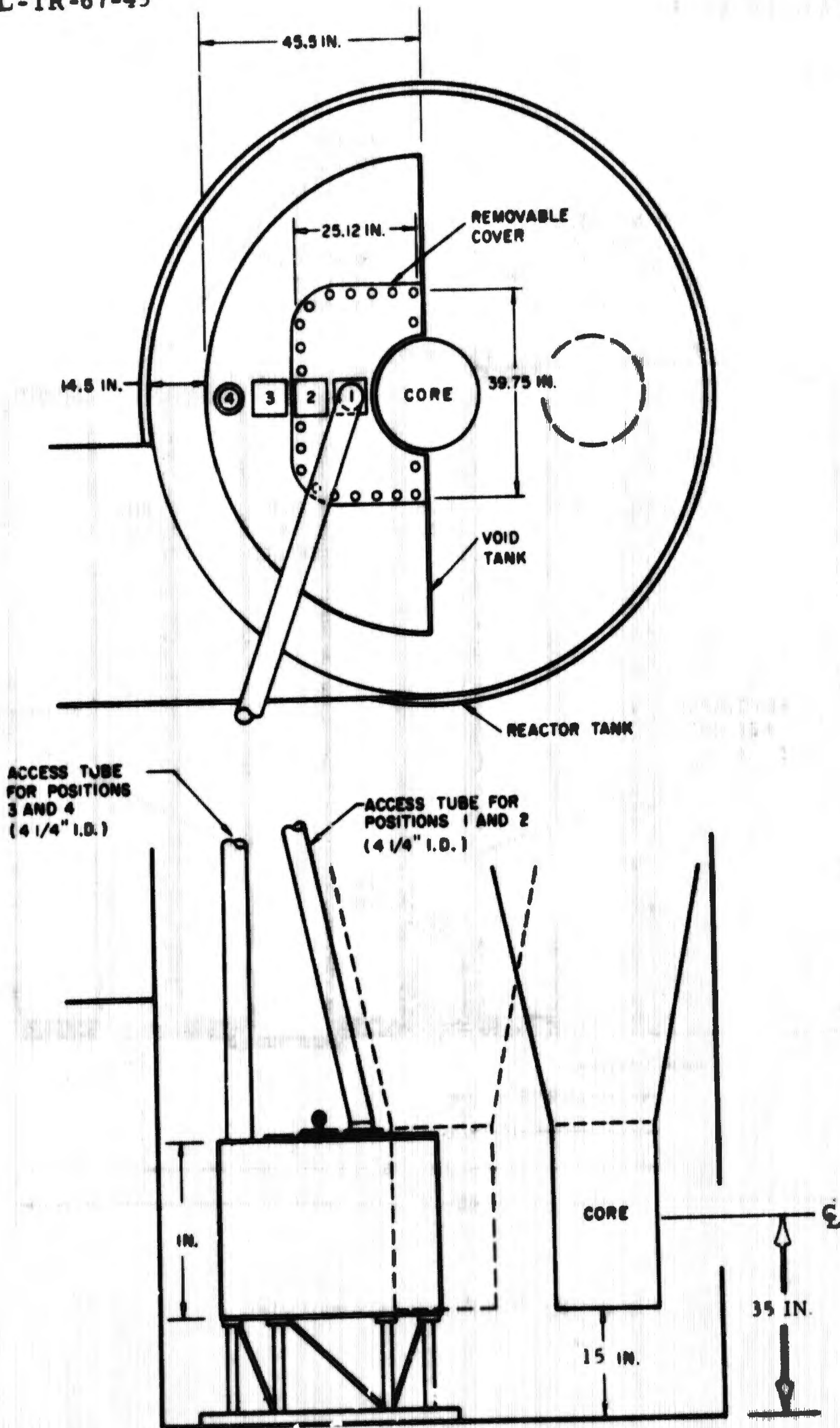

Figure 9. Void-tank position relative to reactor core

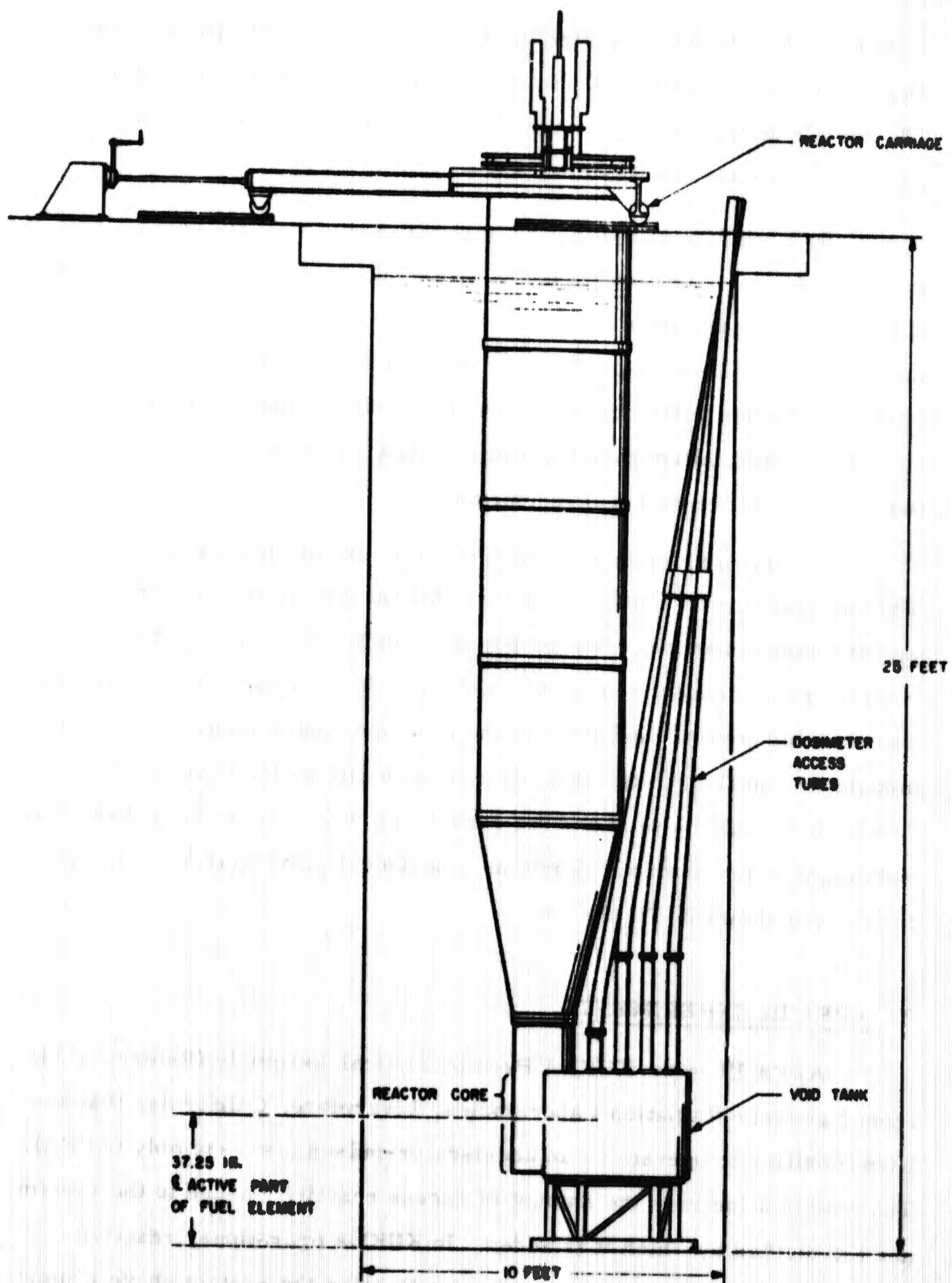

Figure 10. Tank arrangement for ATPR with reactor in position for a void-tank experiment

rotating disk, which was slotted to chop the light at a 50-cps rate with equal on and off periods of 10 msec, was mounted in front of the light. The sample under test was mounted on the other end of the aluminum tube, which was inserted into the void tank.

Bulk lifetime samples were tested in the circuit shown schematically in Figure 11. As the photoconductivity signal, ΔV, was a modulated signal, it could be detected and monitored with an ac-coupled amplifier and thus the bridge circuit of Figure 5 was unnecessary. The shift of the dc level at the irradiation pulse caused a zero-level shift in the ΔV signal. This zero-level shift, although bothersome in data reduction, did not impair the accuracy of the data measurements.

Silicon solar cells were tested in the circuit shown in Figure 12. The value of R_L was chosen to ensure that the parameter being measured was the short-circuit current output of the cell. For these tests, this resistor value ranged from 20 to 60 ohms. Here, again, the anneal data was obtained from the envelope of the light-modulated signal, but as the modulated signal was not superposed on a relatively large dc level, dc-coupling could be used and the zero-level shift seen in the bulk-sample photosignals was avoided. Portions of a typical solar-cell oscillograph record are shown in Figure 13.

3. APFA III EXPERIMENTS

APFA III is the KUKLA Prompt Critical Assembly (Reference 14) from Lawrence Radiation Laboratories, Livermore, California, that has been modified to operate as an accelerator-pulsed fast assembly (APFA). The modification is in the amount of excess reactivity added to the system and the method by which it is added. In KUKLA operations, reactivity is added rapidly by means of an air ram to bring the system above prompt critical. For APFA III, the reactivity is added slowly by means of a mechanical drive mechanism to bring the system to less than prompt

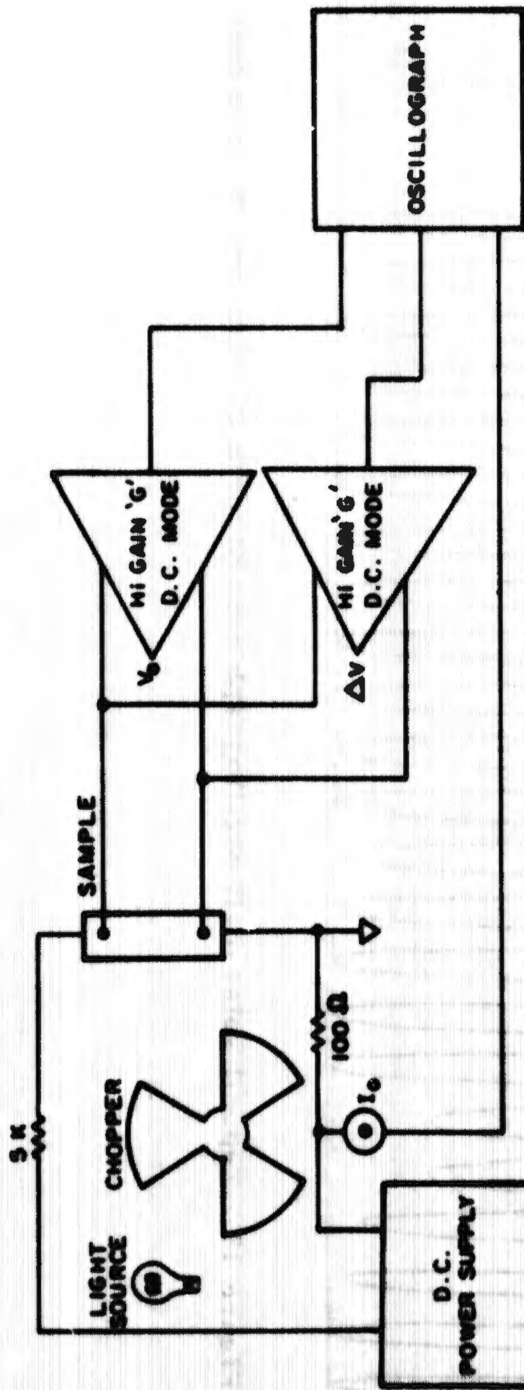

Figure 11. Schematic of bulk photoconductivity sample test circuit

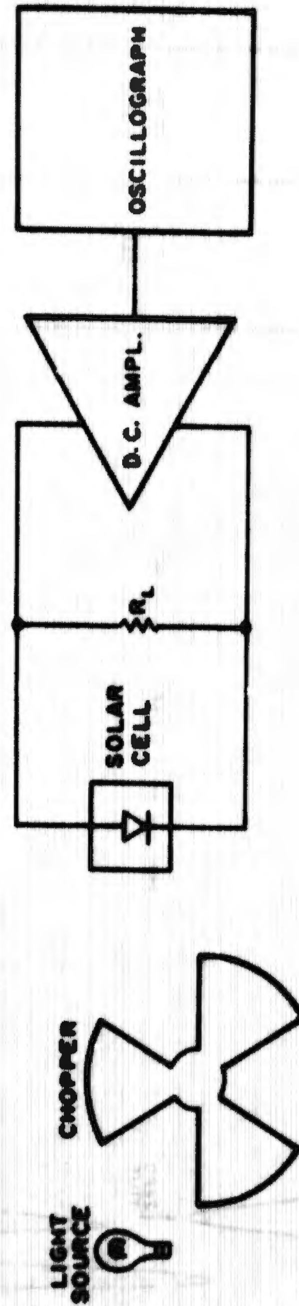

Figure 12. Schematic of silicon sclar cell test circuit

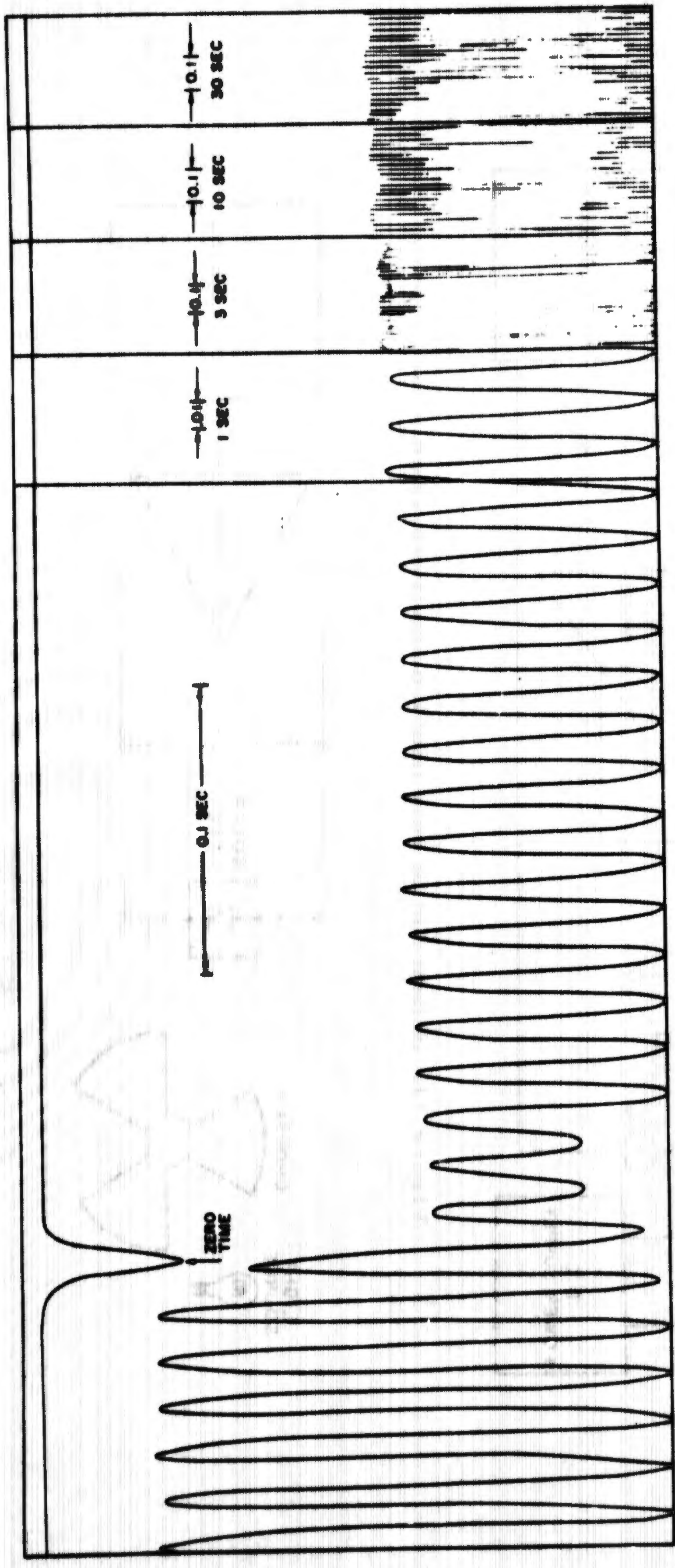

Figure 13. Typical solar-cell oscillograph record for a 10-ohm-cm, p-base cell

critical. The electron beam is fired into the assembly to create a source of neutrons through (γ, n) and (γ, f) reactions of bremsstrahlung radiation and the neutrons are then multiplied by the reactor to create an intense pulse of prompt neutrons. The prompt-neutron pulse is governed by the electron linear accelerator (Linac) pulse and the prompt neutron period.

Physically, APFA III is a bare spherical assembly fabricated from approximately 60 kg of 93 percent enriched uranium. The assembly was designed to have a minimum void space and minimum structural members within the fuel assembly. Figure 14 is a sketch of the APFA III assembly and Figure 15 is a sketch of the APFA III sphere as it would look disassembled.

The neutron yield of APFA II, the predecessor of APFA III, was measured at several reactivities ranging from subcritical to supercritical. The APFA III yield has not been studied as thoroughly yet, but it will be the same as for APFA II for the same range of Linac parameters. The measurements were made with sulfur threshold detectors and a long counter calibrated with a standard neutron source. The electron-beam current was measured with a secondary-emission monitor. With sulfur detectors, the fluence above 3 Mev was measured. The neutron spectrum in the APFA is a degraded fission spectrum and the neutron flux greater than 3 Mev is 14 percent of the total neutron flux. This factor was obtained using experimental data of Rosen, et al., on GODIVA (Reference 15), and the Goldstein and Carlson (Reference 16) function $\sqrt{E}\,\exp(-0.775\,E)$. It is assumed that for energies greater than 3 Mev, the neutron spectrum is essentially a fission spectrum, so the analytical function was normalized to the experimental-data curve at this energy, as plotted in Figure 16. The experimentally determined yield averaged from both the sulfur foils and the long counter was 0.015 neutrons/electron at a beam energy of 29 Mev. The pulse shape, as determined from a PIN silicon detector meas-

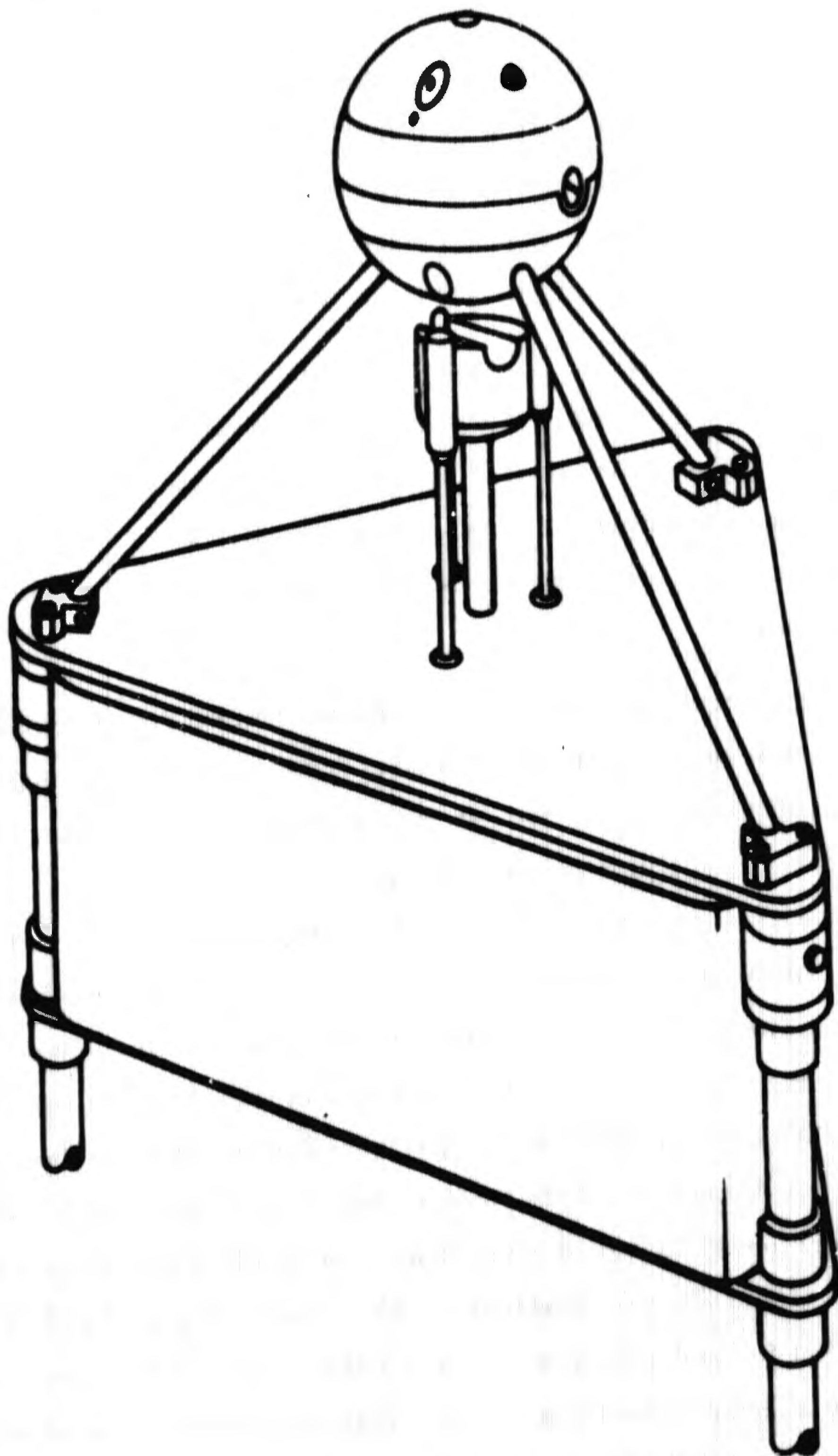

Figure 14. Sketch of APFA assembly

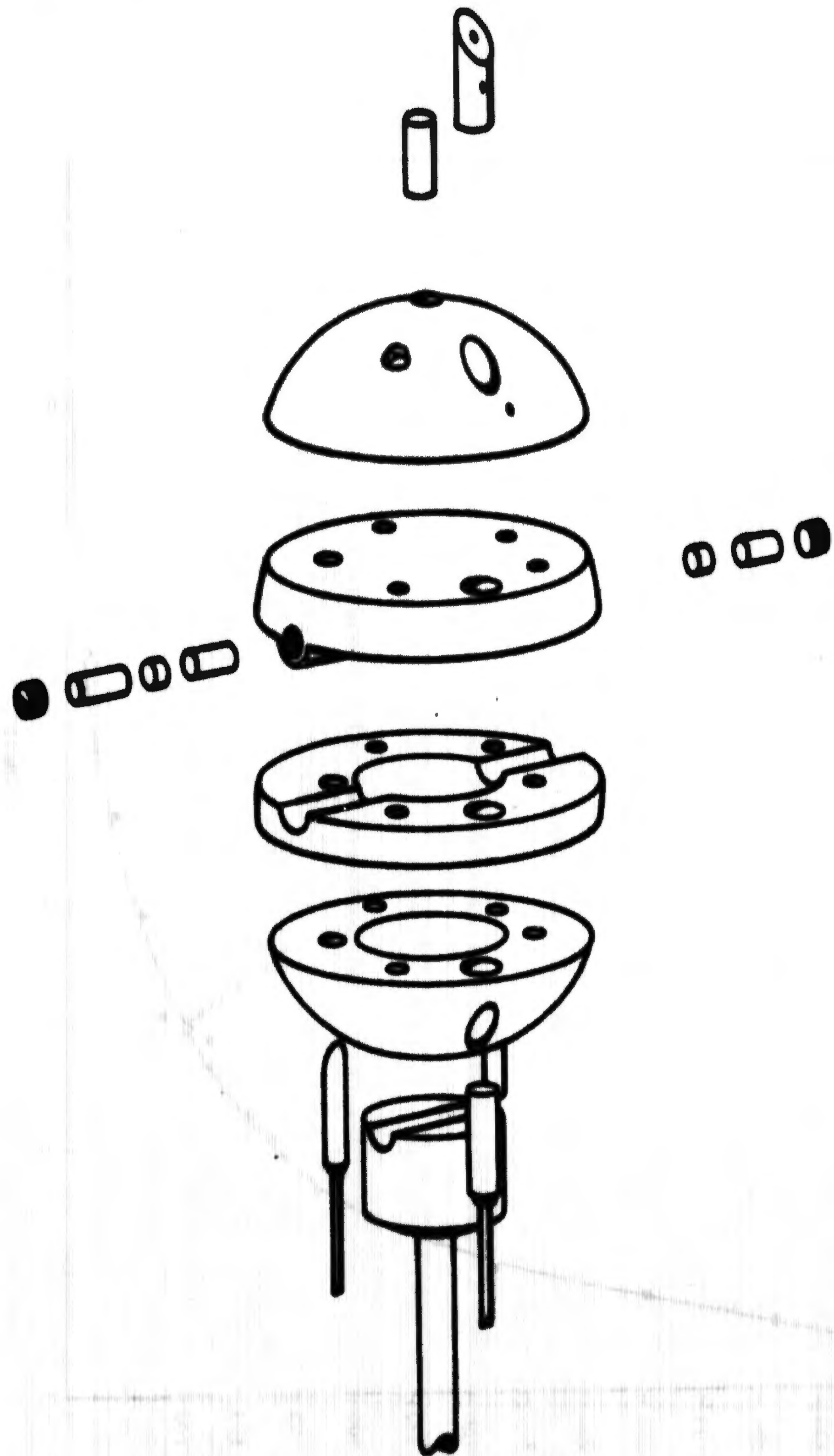

Figure 15. Disassembled view of APFA I

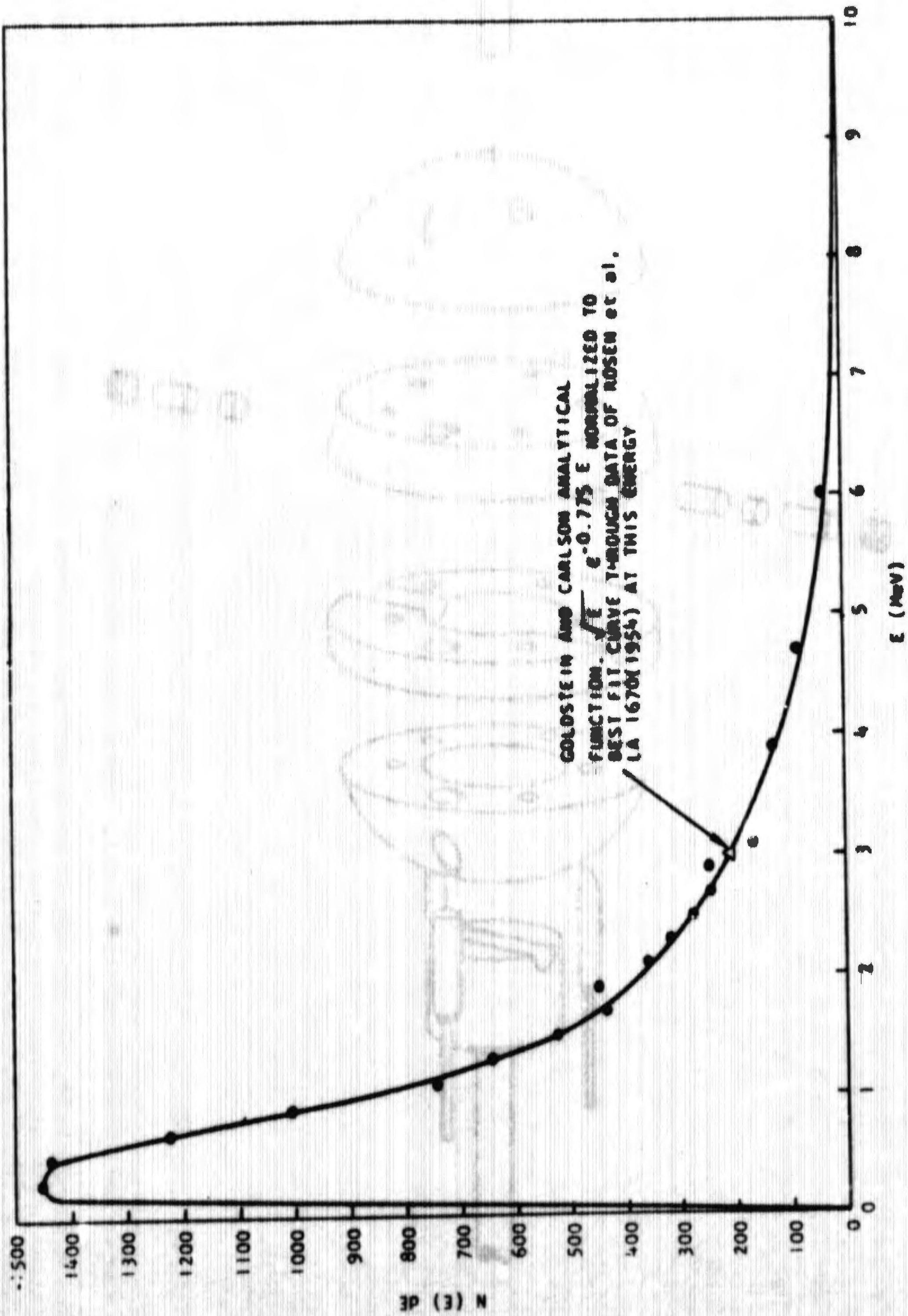

Figure 16. N(E) dE vs E for GODIVA-type reactor (bare critical assembly)

urement of the gamma flux emitted during the pulse, is shown in Figure 17 along with the 4-μsec, 29-Mev electron-beam pulse which initiated this neutron pulse.

Only preliminary solar-cell tests have been performed in APFA III to date. These tests used the circuit of Figure 18. The amplifier system used consists of a preamplifier followed by a replacement vertical amplifier for a Type 545 oscilloscope with a specially designed direct-coupled cathode-follower output stage. This cathode-follower circuit was needed to drive the 250 ft of 93-ohm terminated cable between the APFA Fast Spectrum Cell (FSC) and the experiment monitor station. The data were recorded on oscilloscopes at the monitor station. The gate circuit of Figure 19 was necessary to keep the amplifier from saturating with the large signal generated by the ionization during the Linac-neutron pulse. Using a balanced load and taking differential measurements throughout the system served to minimize noise problems. Figure 20 shows the noise level observed in the preliminary tests.

A sketch of the setup for the APFA experiments is shown in Figure 21. Because of the low neutron yield of the APFA III with the present linear accelerator capabilities, all experiments in the early stages will have to be performed inside the APFA sphere, and since space is limited for this mode of operation, cooling of the sample for the low-temperature experiments will be difficult. To date, the Atomic Energy Commission has not granted permission to flow liquid nitrogen through the cooling lines, so the less-efficient method of using an exchange gas will have to be used.

As the APFA III was not ready for use until quite late in the contract period, the only tests performed were at room temperature during the preliminary checkout of the APFA assembly.

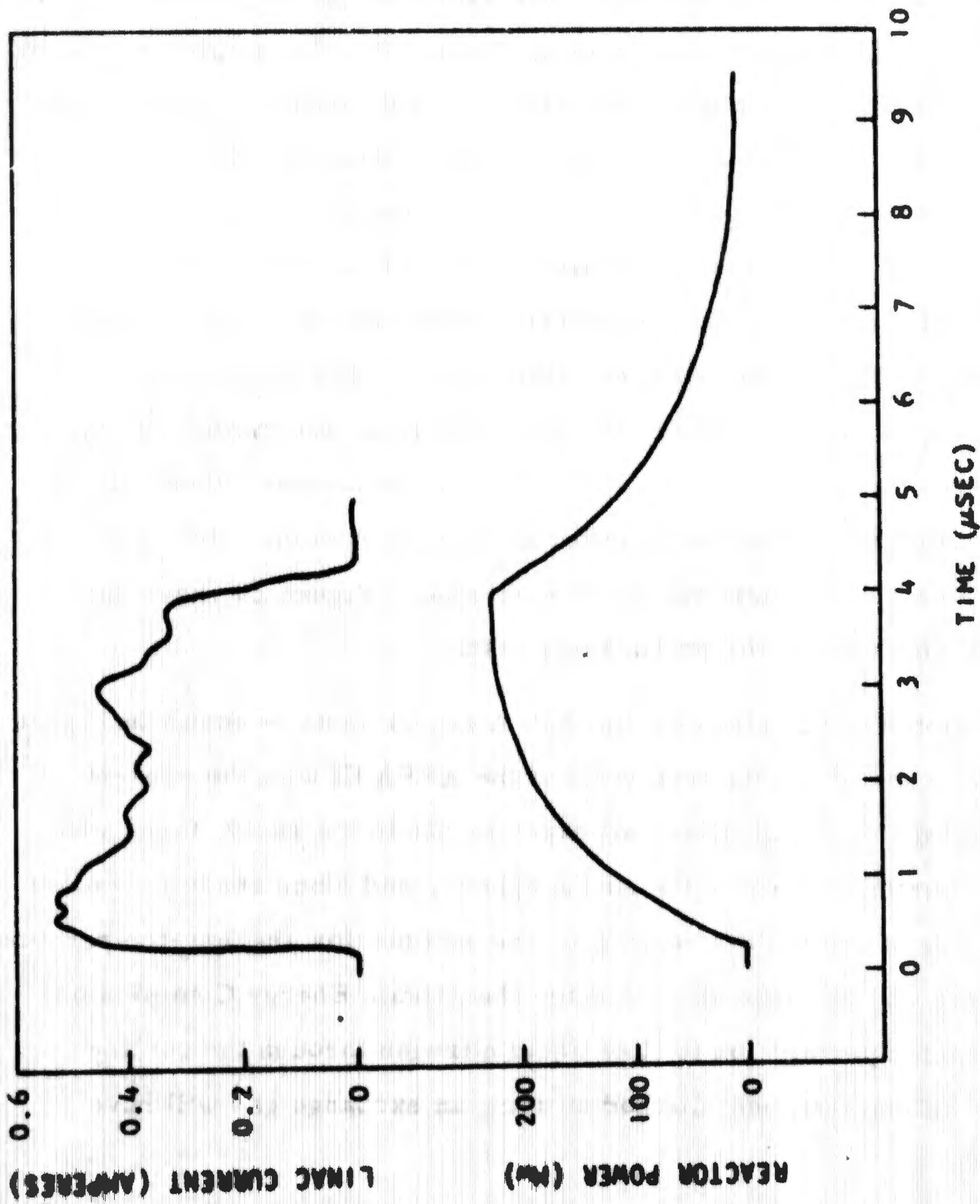

Figure 17. APFA burst shape and Linac beam pulse for prompt multiplication of 250

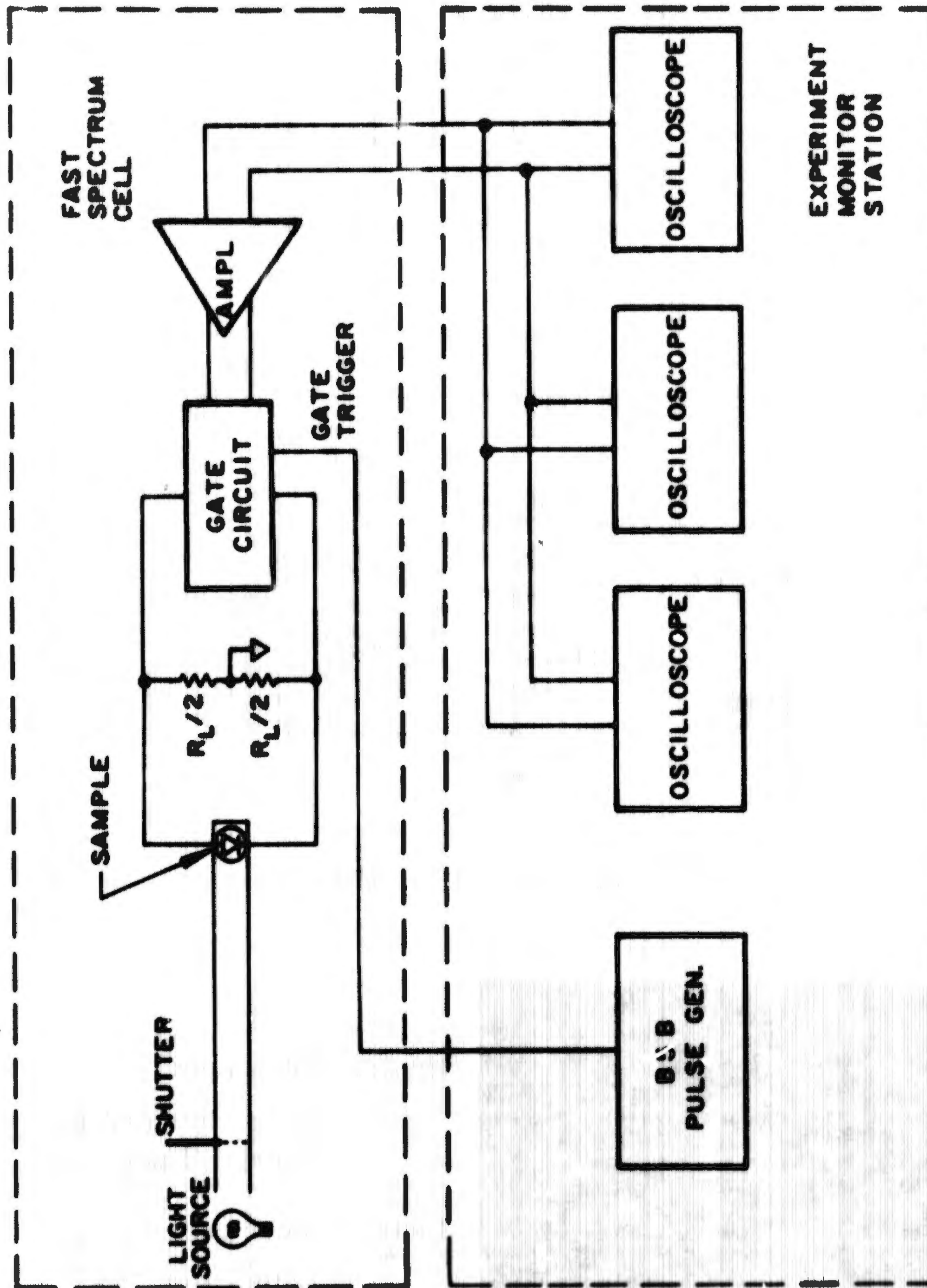

Figure 18. Test circuit for APFA tests

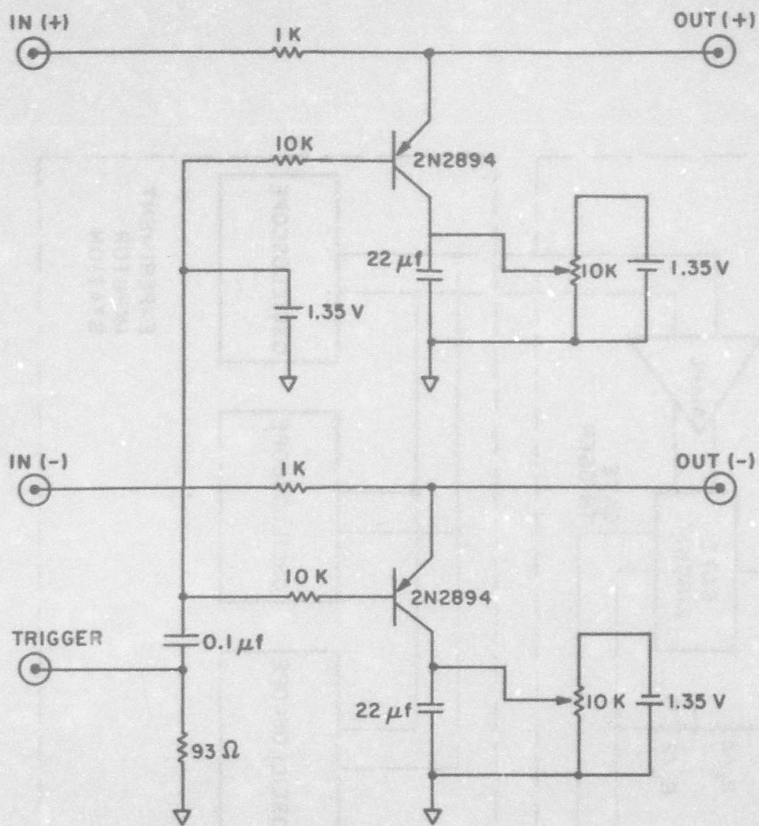

Figure 19. Gate circuit for APFA tests

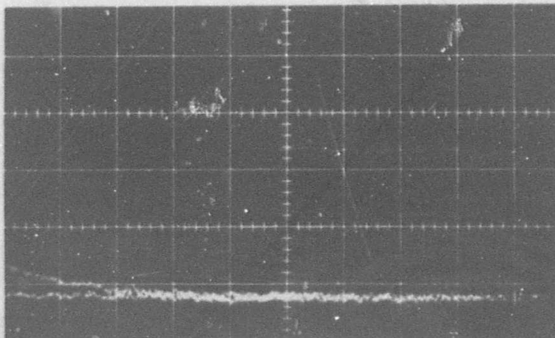

Upper: PIN output

Gain: 100 mv/div
Sweep: 2 μsec/div

Lower: Solar cell

Gain: 1 mv/div
Sweep: 10 μsec/div

Figure 20. Noise signal in solar-cell test circuit for APFA experiments

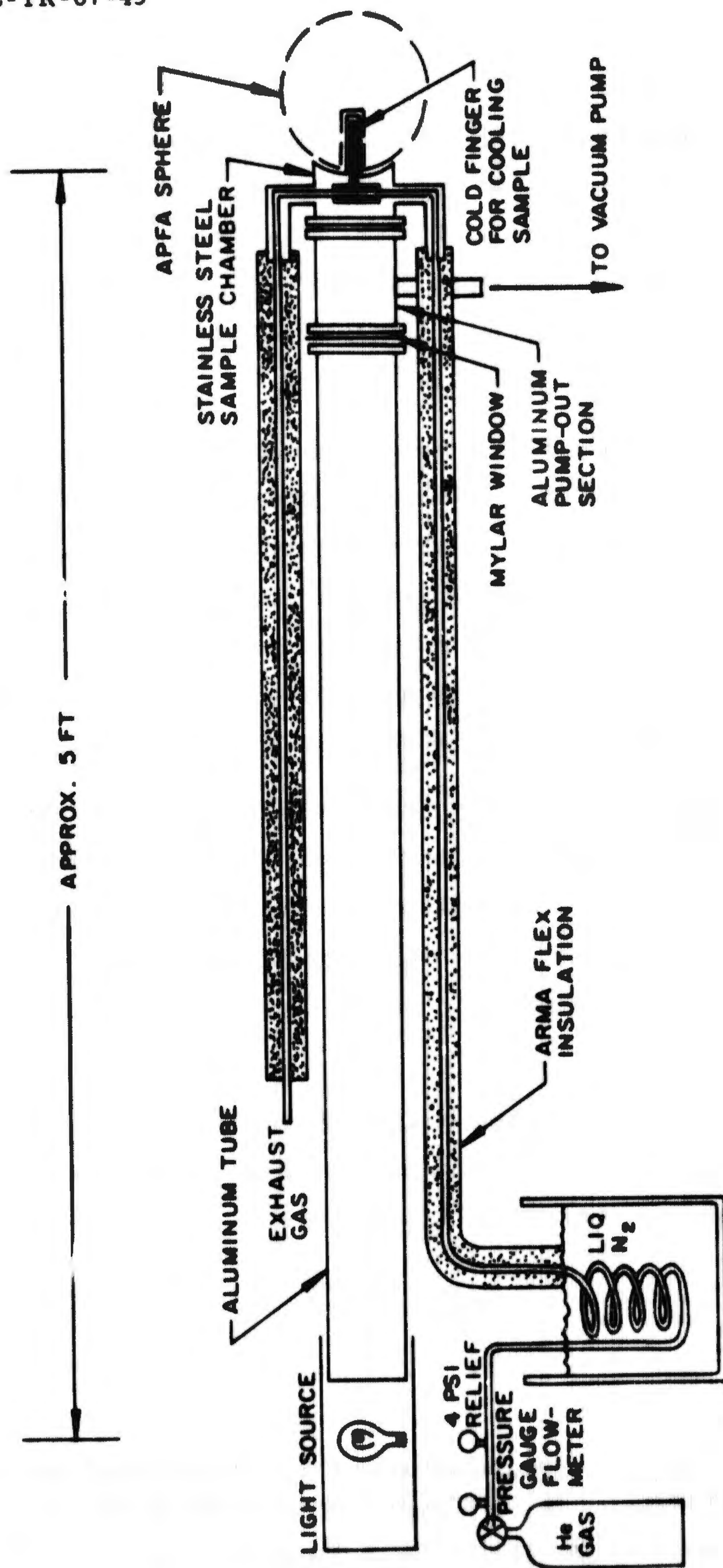

Figure 21. Experiment configuration for APFA tests

4. SAMPLES

Conductivity and bulk photoconductivity samples were standard four-probe silicon or germanium bar-type samples approximately 1.5 cm long and 2 mm by 4 mm in cross section. The voltage probes were spaced 1 cm apart. All samples were single crystal; they were sliced from their parent boules with a diamond saw, apped on successively finer-grit emery papers, and chemically etched in CP-4.*

Current and voltage probes were attached to both n- and p-type germanium using an indium-alloy solder and a special flux. Contacts to n-type silicon were made by alloying a preform† to the sample at a temperature of 450°C in a forming-gas atmosphere. Leads were then soldered to the alloy contacts. Current contacts to the p-type samples were solder contacts to rhodium-plated end regions. Voltage probes were thermocompression-bonded doped-gold leads bonded to evaporated aluminum contacts.

These sample contacts showed, at most, a few percent rectification at room temperature. However, this does not preclude the production of sizable photovoltages at these contacts. As a recent publication (Reference 17) has stated, "Actually, it is virtually impossible to make a contact between metal and a semiconductor which will not produce a contact photo-emf. . . ."

The solar cells used in these tests were commercial units from two different manufacturers. They were 1 cm by 2 cm in area, about 0.013 inches thick, and had sintered Ti-Ag contacts.

*CP-4 etching solution: 6 ml glacial acetic acid, 10 ml concentrated nitric acid, 6 ml of 48 percent hydrofluoric acid, and 5 drops of bromine water.

†Preform composition: 98.9 percent Au, 0.1 percent As, 1 percent Si.

SECTION V
EXPERIMENTAL RESULTS

1. CONDUCTIVITY SAMPLES

The first investigations of short-term anneal effects were made by monitoring conductivity changes in standard, four-probe, rectangular samples of single-crystal semiconductor materials. These investigations were not very productive as the short-term anneal of conductivity proved to be slight and of a "reverse anneal" type, i.e., the material damage appears to increase with time following an irradiation. This is contrary to observed device parameter changes and to minority-carrier lifetime changes observed in bulk samples. Results of the conductivity anneal experiments in samples of bulk semiconductor materials which were conducted in the ATPR J-tube facility (Figure 5) are plotted in Figure 22. These conductivity measurements were discontinued early in the program so that effort could be concentrated on short-term anneal of minority-carrier lifetime, which is more sensitive to irradiation and more significant to the operation of semiconductor devices. It soon became obvious that the damage center responsible for radiation dependence of minority-carrier lifetime was not the same as that responsible for carrier removal as the two parameters showed different time constants.

The strange time behavior of the conductivity of the quartz-crucible (QC) grown, 7-ohm-cm phosphorus-doped silicon sample is not understood, but this same characteristic behavior was observed in three separate tests on this material. The germanium samples seem to show an initial reverse anneal followed by a small forward anneal. Neither n-type nor p-type floating-zone (FZ) grown silicon samples showed this reversal.

2. BULK PHOTOCONDUCTIVITY SAMPLES

Minority-carrier lifetime measurements were attempted on standard four-probe samples of n- and p-type single-crystal silicon and germanium. Although the measurements were difficult to make because of the low signal-to-noise ratio encountered in monitoring the small photosignals and the obfuscating

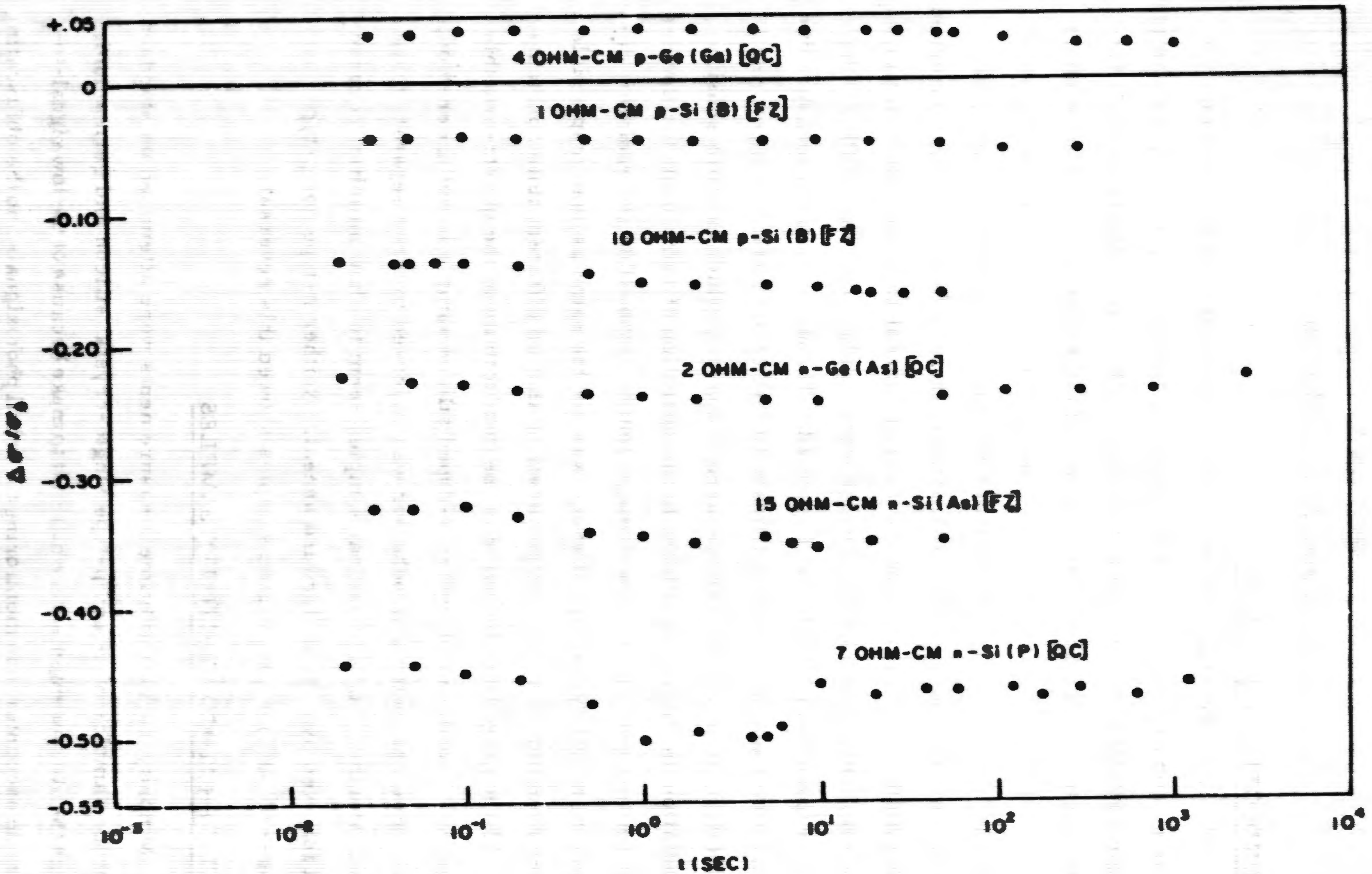

Figure 22. Change in conductivity vs time for bulk semiconductor samples following exposure to ≈ 4.5 x 10^{13} nvt pulses in the J-tube of the ATPR facility

effects of contact photovoltages, data were obtained on all but the p-type silicon sample. These data are shown in Figures 23 through 26 in terms of both the R parameter, discussed in Section III, and an annealing factor. The significance of this annealing factor is discussed in the Appendix. All samples show an anneal which is essentially complete by 2 sec or earlier.

3. SILICON SOLAR CELLS

The most extensive tests were performed on silicon solar cells. These experiments, which were performed primarily in the void tank location of the ATPR facility with approximately 2×10^{12} neutrons/cm^2 pulses, provide minority-carrier lifetime anneal data from about 10 msec on. Cells manufactured by two different manufacturers were used. The parameter measured was the short-circuit current output of the cells. These data are plotted in Figures 27 through 37 in terms of the time dependence of both the ratio of the radiation-induced to initial recombination-center concentration, R, or the annealing factor.

Figure 27 shows R versus t for two n-base solar cells made from phosphorus-doped, QC-grown material. One is 1-ohm-cm material and the other is 0.1 ohm-cm. Both show identical behavior. These data are presented in Figure 28 in terms of the anneal factor, where the 1-ohm-cm sample shows a slightly larger anneal than the 0.1-ohm-cm sample.

Figures 29 and 30 show annealing for three n-base solar cells made from arsenic-doped, QC-grown material. The resistivities of the base material for these three cells are 0.1, 1, and 10 ohm-cm. These cells showed stronger annealing in the higher-resistivity material but practically none in the 0.1-ohm-cm sample.

The plot of the annealing factor of another 10-ohm-cm arsenic-doped solar cell in Figure 31 shows an annealing factor at 10 msec of about 1.18. Annealing factors at 10 msec for other silicon solar cells tested are tabulated in Table VI.

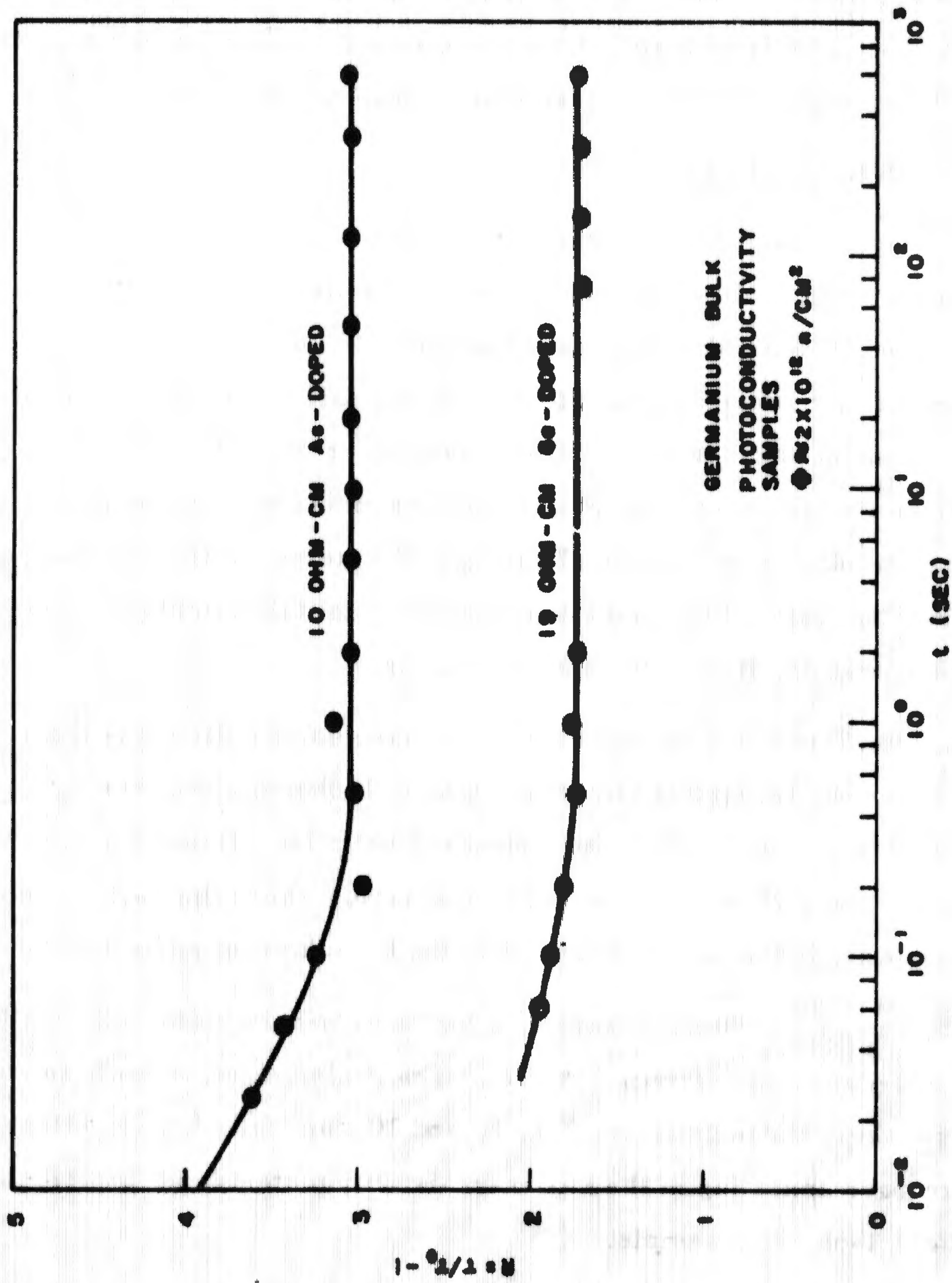

Figure 23. Time dependence of the ratio of radiation-induced to initial recombination center concentration in germanium bulk photoconductivity samples following a 2×10^{12} n/cm^2 pulse

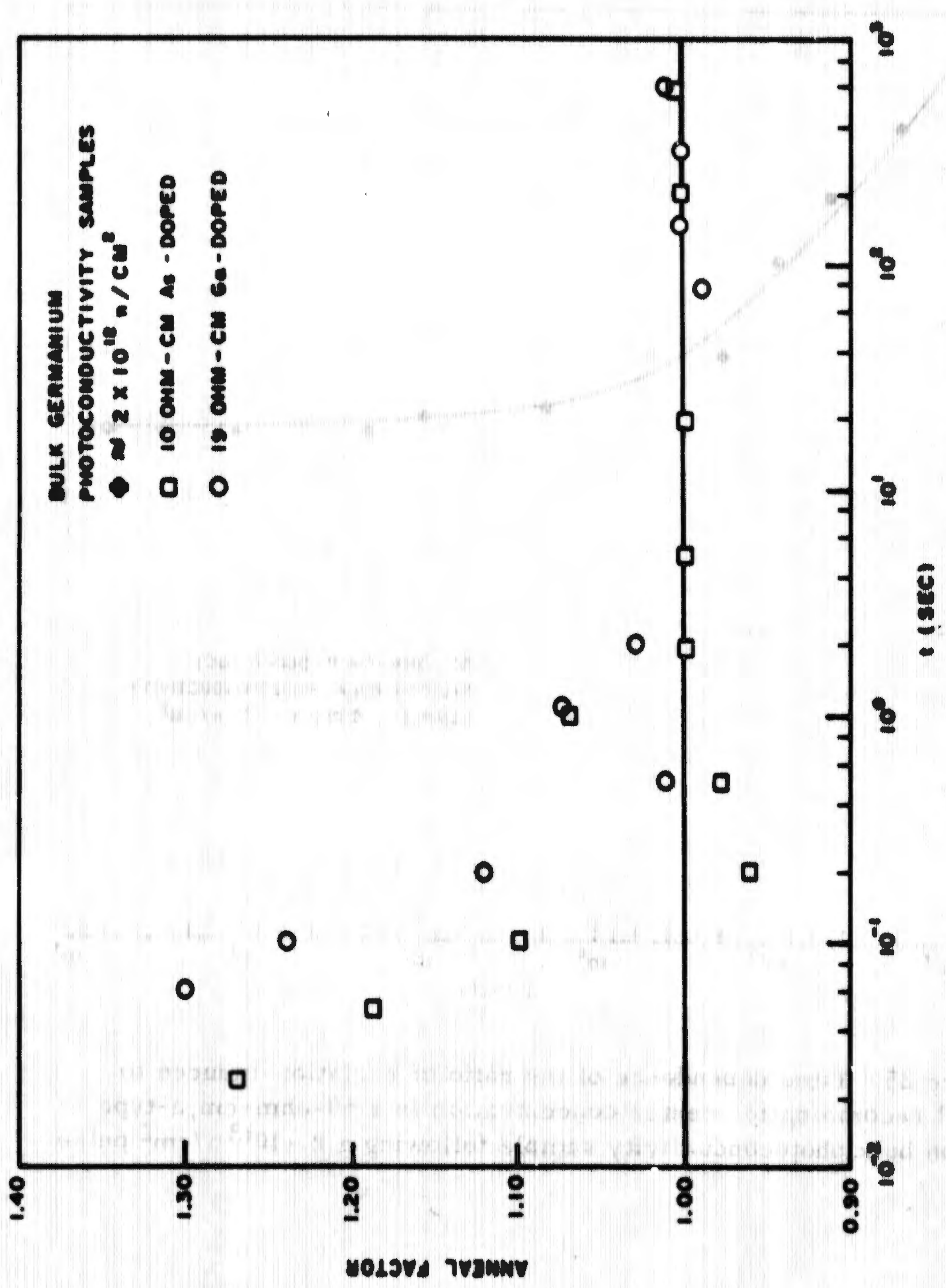

Figure 24. Annealing factor vs time for two germanium bulk photoconductivity samples

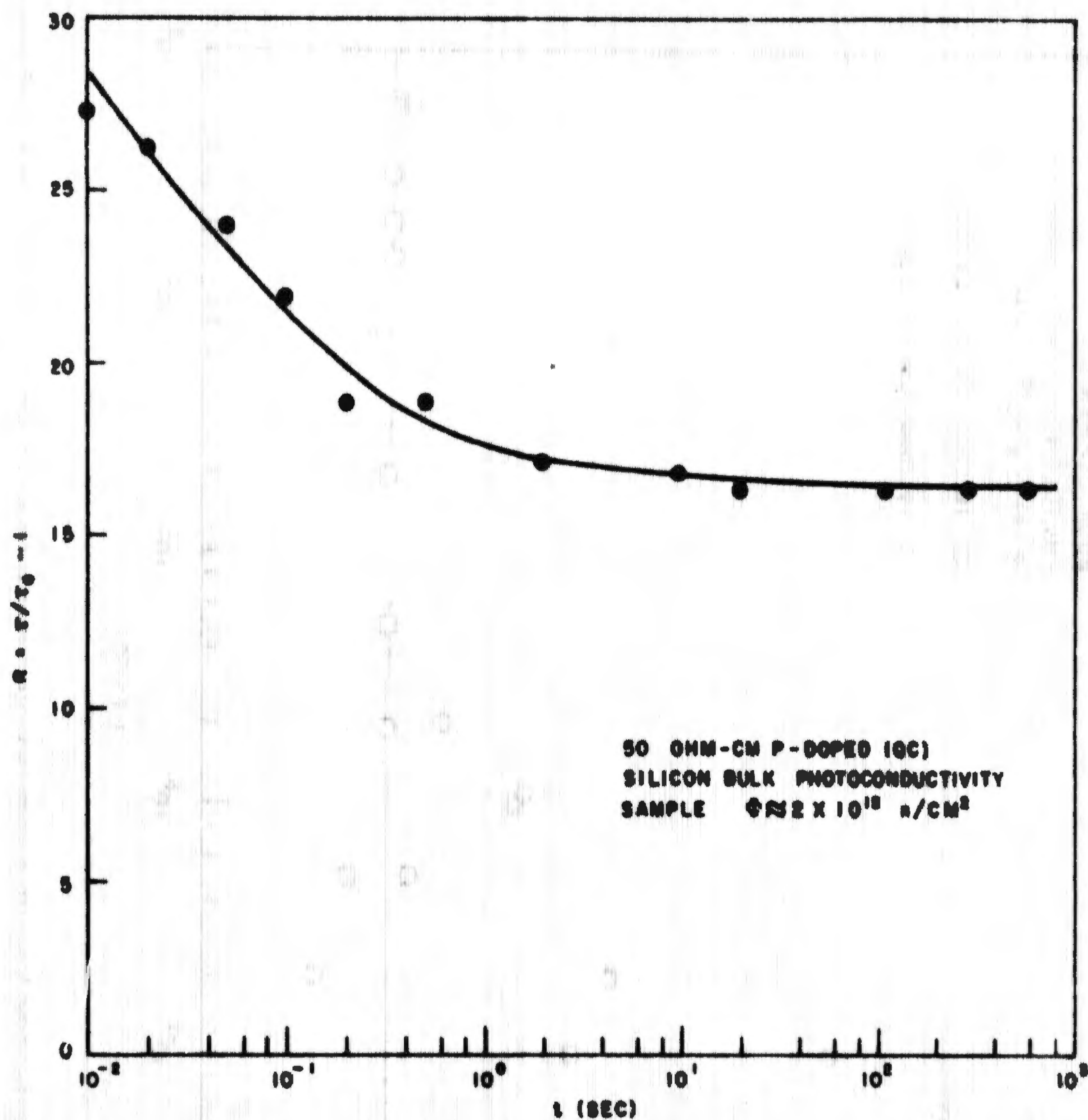

Figure 25. Time dependence of the ratio of radiation-induced to initial recombination center concentration in a 50-ohm-cm, n-type silicon bulk photoconductivity sample following a 2×10^{12} n/cm^2 pulse

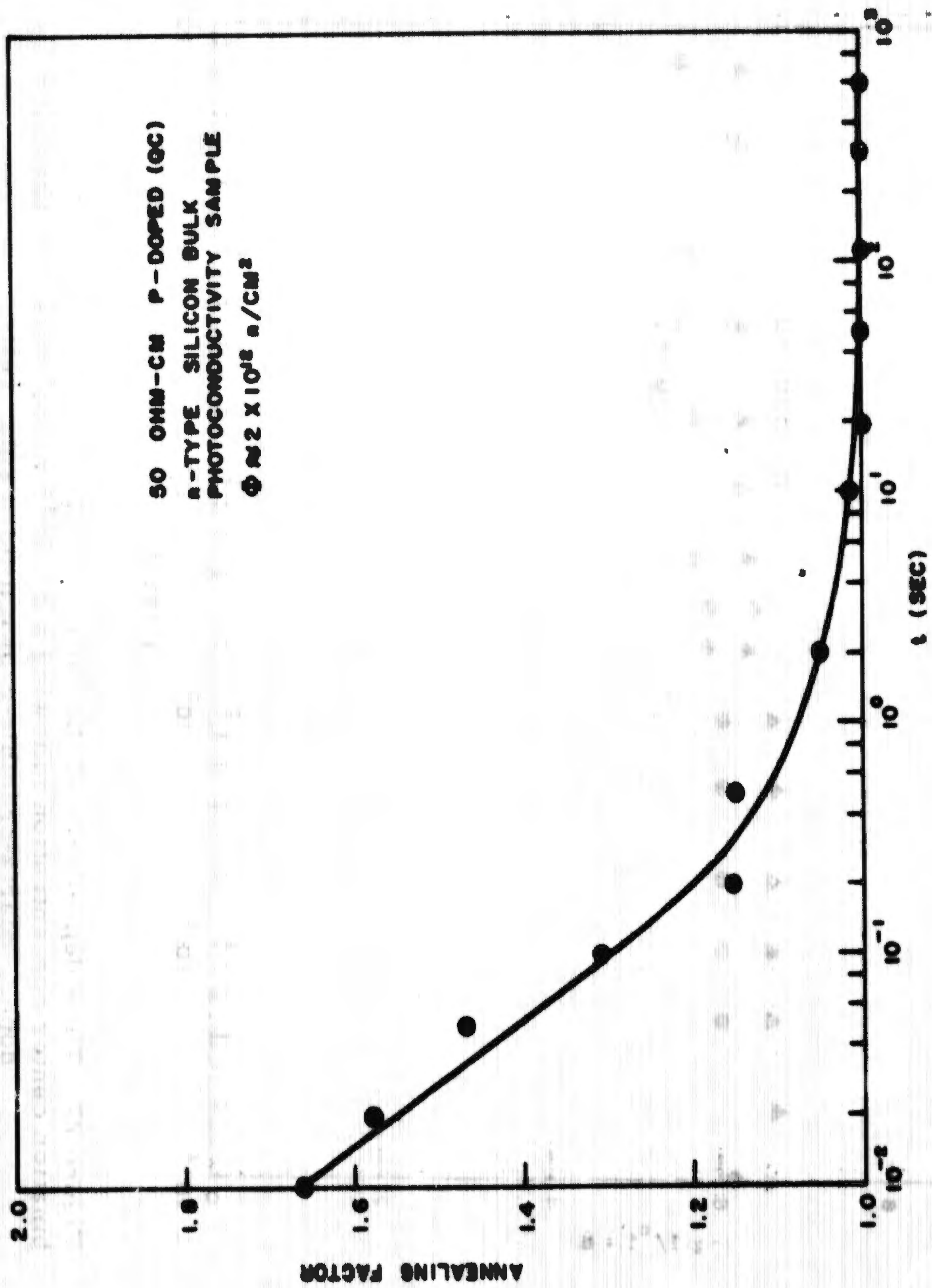

Figure 26. Annealing factor vs time for a 50-ohm-cm, phosphorus-doped, quartz-crucible grown, n-type silicon bulk photoconductivity sample

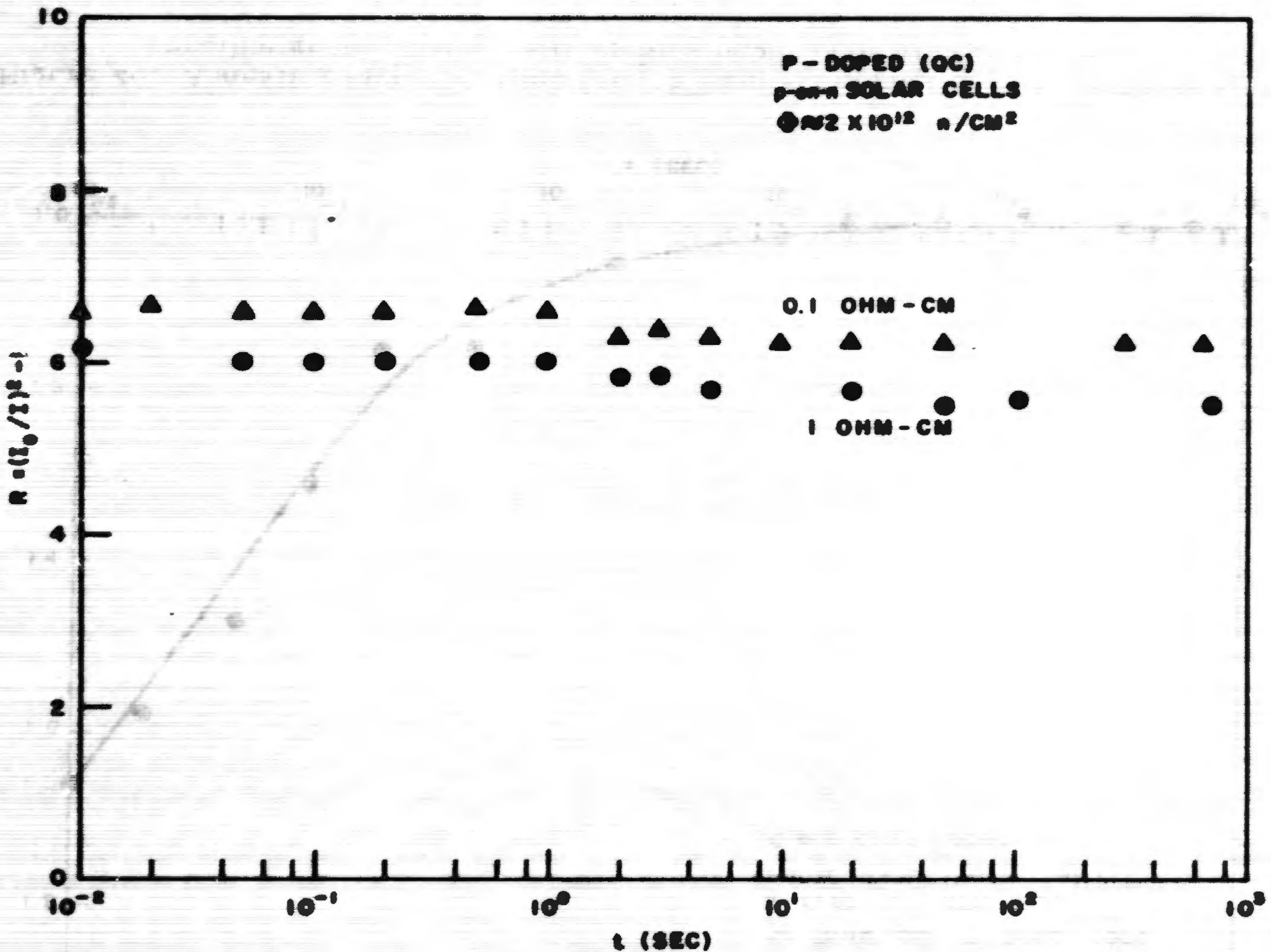

Figure 27. Time dependence of the ratio of radiation-induced to initial recombination center concentration following a 2×10^{12} n/cm^2 pulse for phosphorus-doped, quartz-crucible-grown, p-on-n solar cells

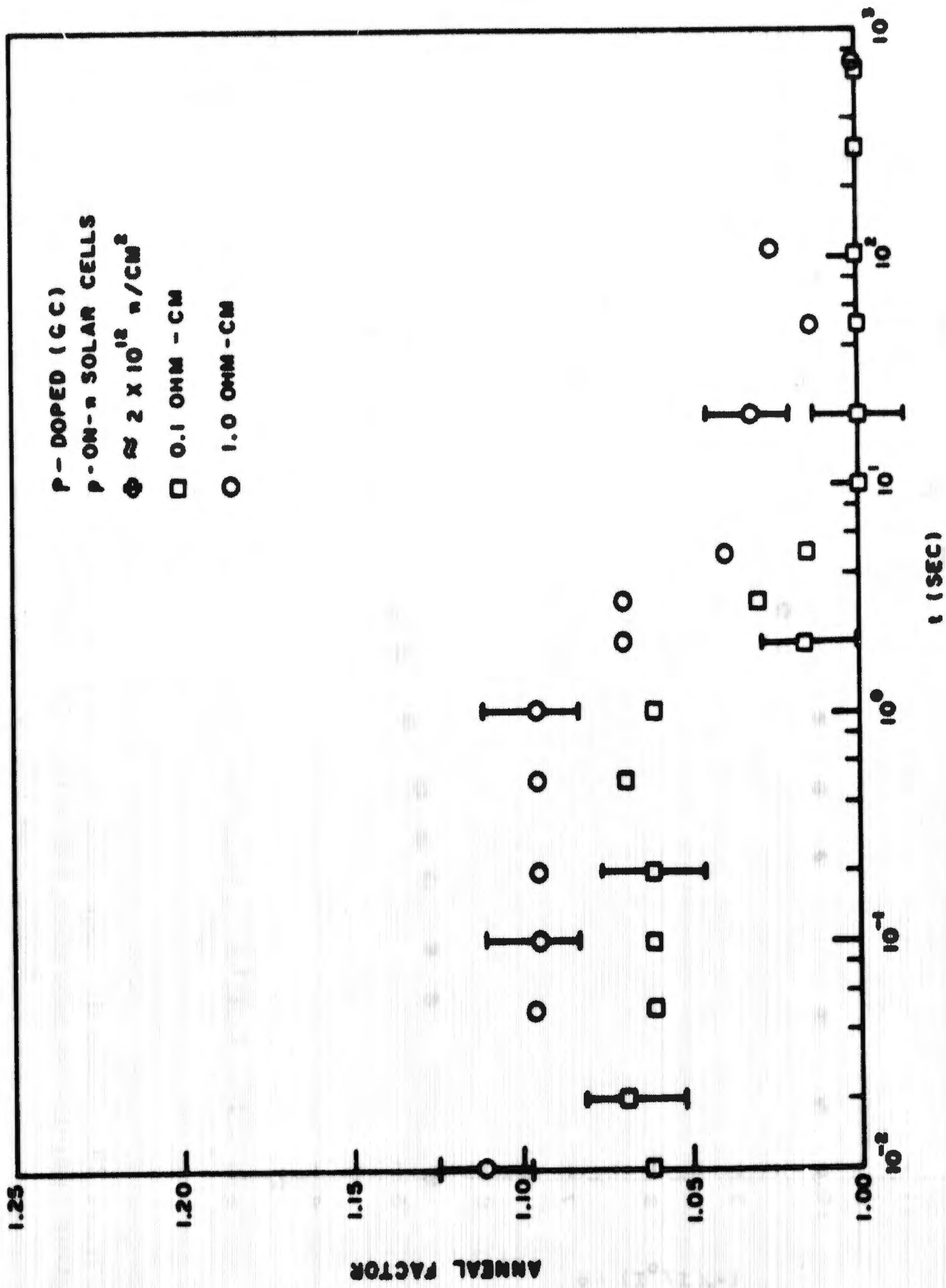

Figure 28. Annealing factor vs time for two phosphorus-doped, quartz-crucible grown, p-on-n solar cells

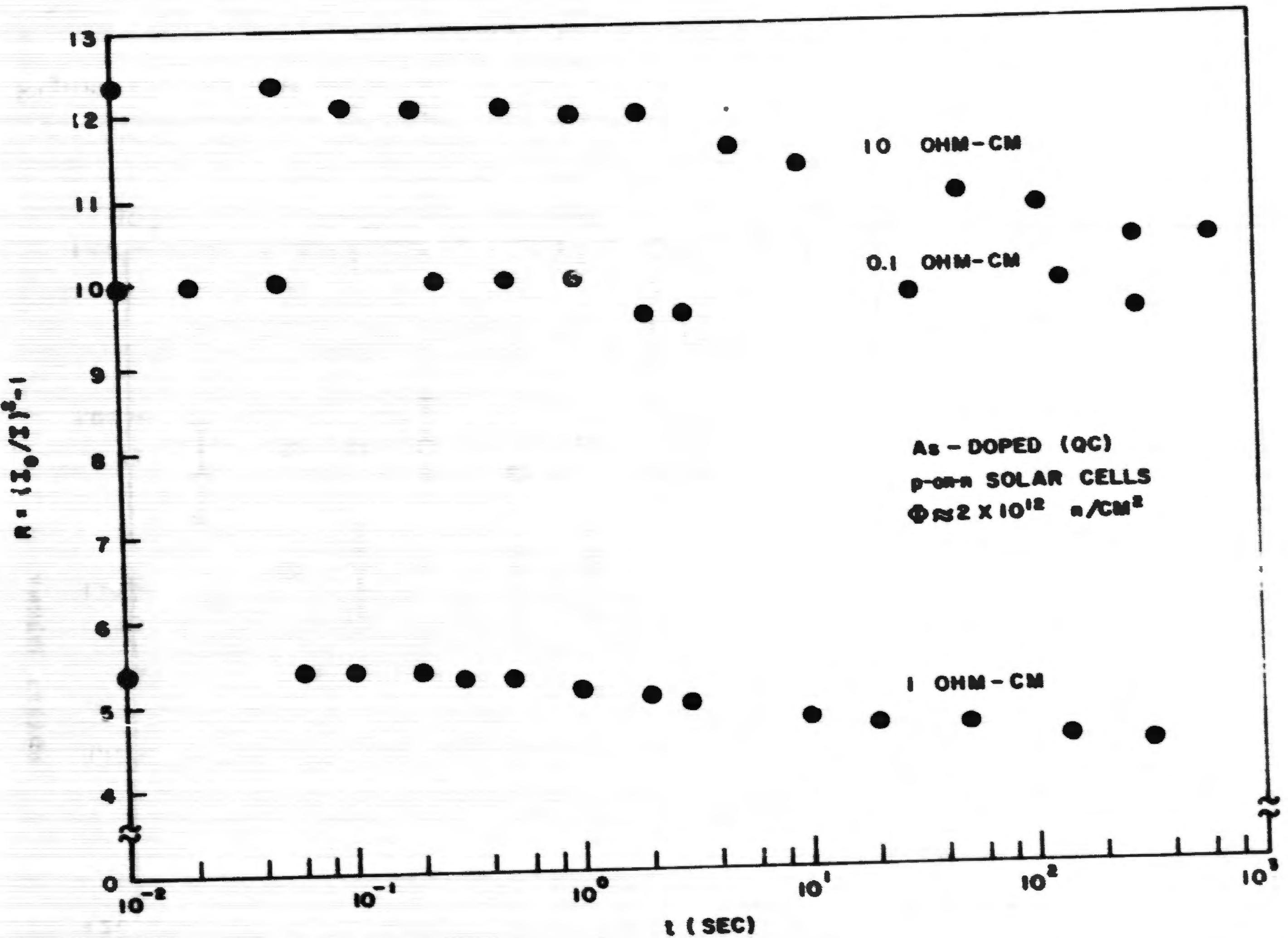

Figure 29. Time dependence of the ratio of radiation-induced to initial recombination center concentration following a 2×10^{12} n/cm^2 pulse for arsenic-doped, quartz-crucible-grown, p-on-n solar cells

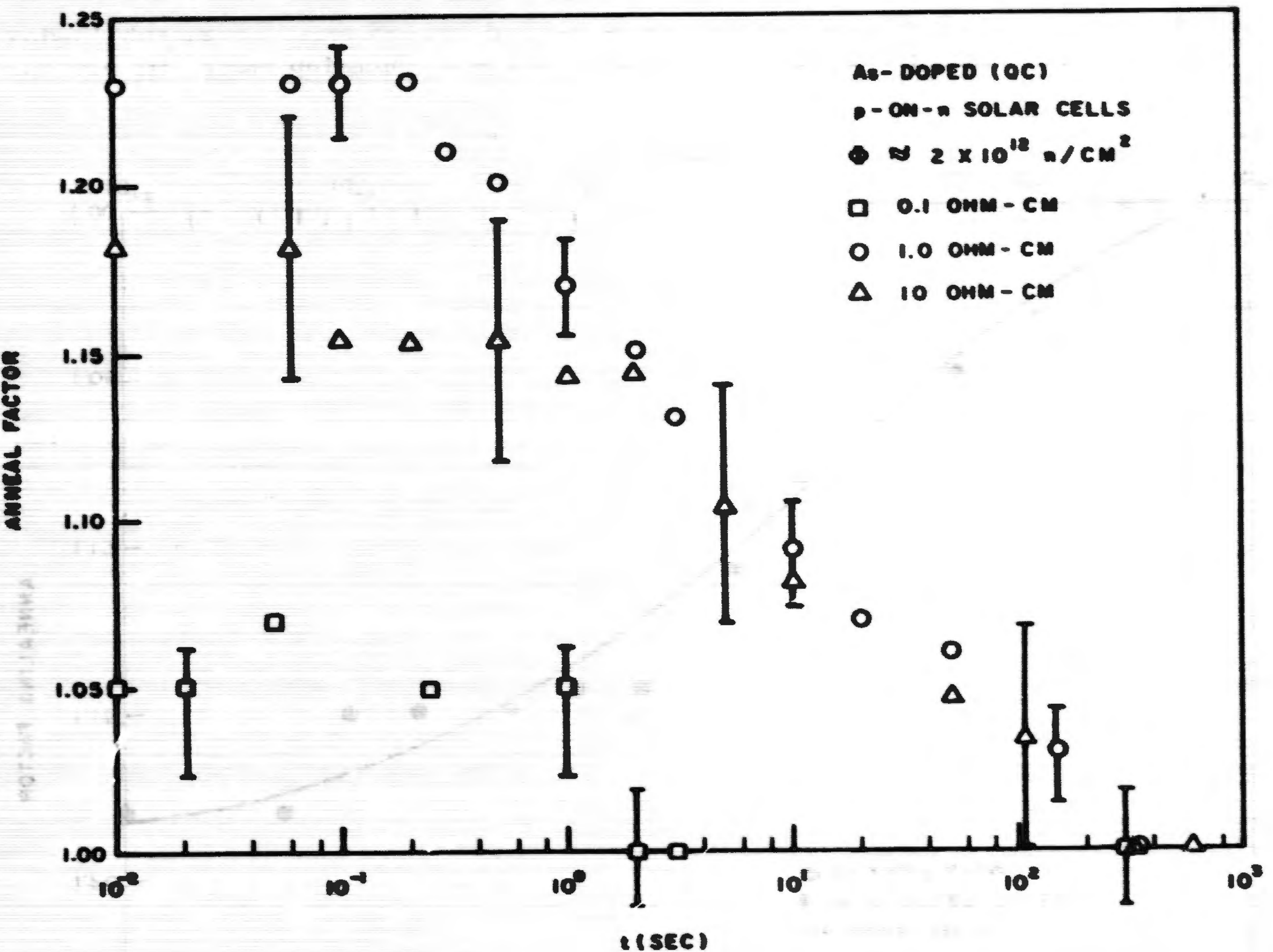

Figure 30. Annealing factor vs time for three arsenic-doped, quartz-crucible grown, p-on-n solar cells

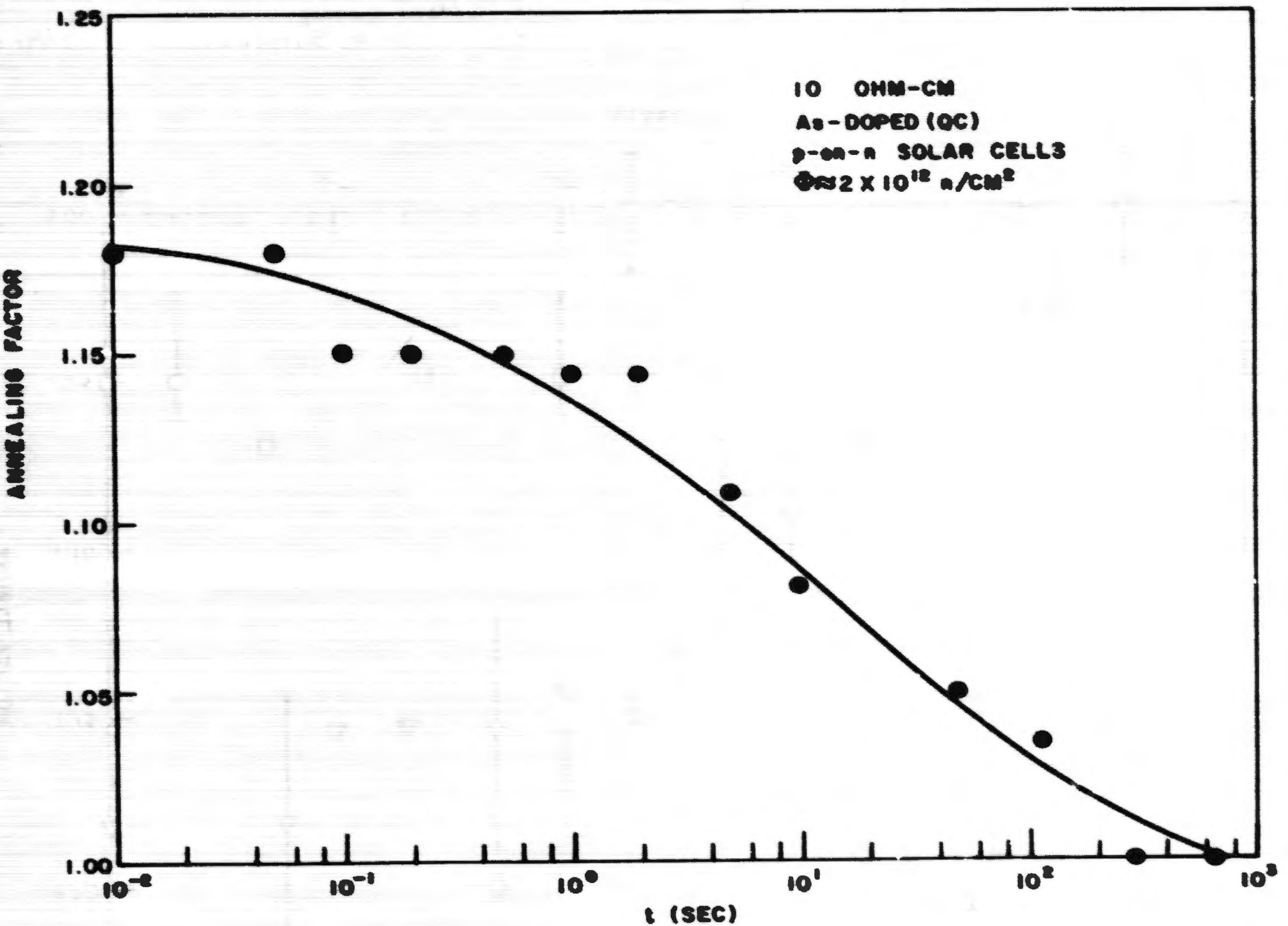

Figure 31. Time dependence of the annealing factor for a 10-ohm-cm, arsenic-doped, quartz-crucible-grown, p-on-n solar cell following a 2×10^{12} n/cm^2 pulse

Table VI

SOLAR-CELL ANNEALING FACTORS

Type	Dopant	Resistivity (ohm-cm)	Annealing Factor
n-on-p	B	1	1.64
n-on-p	B	10	1.6-1.8
n-on-p	Al	1	1.57
n-on-p	Al	10	1.57
p-on-n	P	0.1	1.06
p-on-n	P	1	1.12
p-on-n	As	0.1	1.04
p-on-n	As	1	1.22
p-on-n	As	10	1.18

Figures 32 through 37 show the annealing of some n-on-p cells. Both 1-ohm-cm and 10-ohm-cm samples of boron-doped and aluminum-doped base materials were tested. The boron-doped material was QC grown and the aluminum-doped material was grown by the Lopex technique. The comparison by resistivity of the two different dopant materials using the R parameter (Figures 32 and 33) shows quite similar behavior, although there is a difference in the first two decades, with the data points for the aluminum-doped material falling below those for the boron-doped material in both resistivity ranges. The annealing-factor plots in Figures 34 and 35 show that there is no difference between the resistivity types, but the shapes of the annealing-factor curves for the two different dopants appear dissimilar.

Figures 36 and 37 show the annealing in terms of R and annealing factor for two 10-ohm-cm boron-doped n-on-p cells. Cell 1 was annealed in the usual way with the light on continuously. Cell 2 was annealed for most of the test period in the same manner, except between 1.8 sec and 9 sec when the light was turned off. The annealing was slight during this

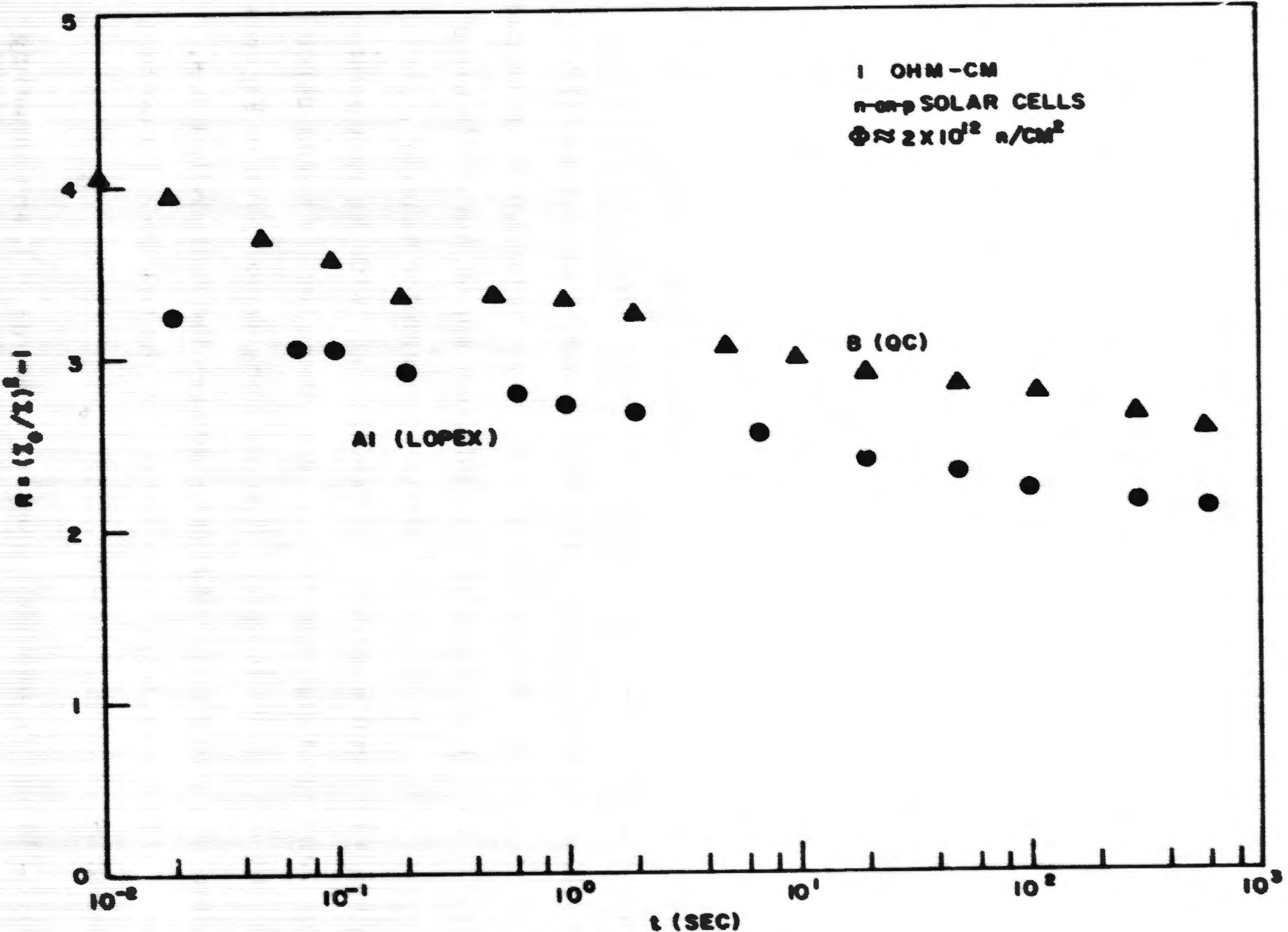

Figure 32. Time dependence of the ratio of radiation-induced to initial recombination center concentration following a 2×10^{12} n/cm^2 pulse for some 1 ohm-cm, n-on-p solar cells

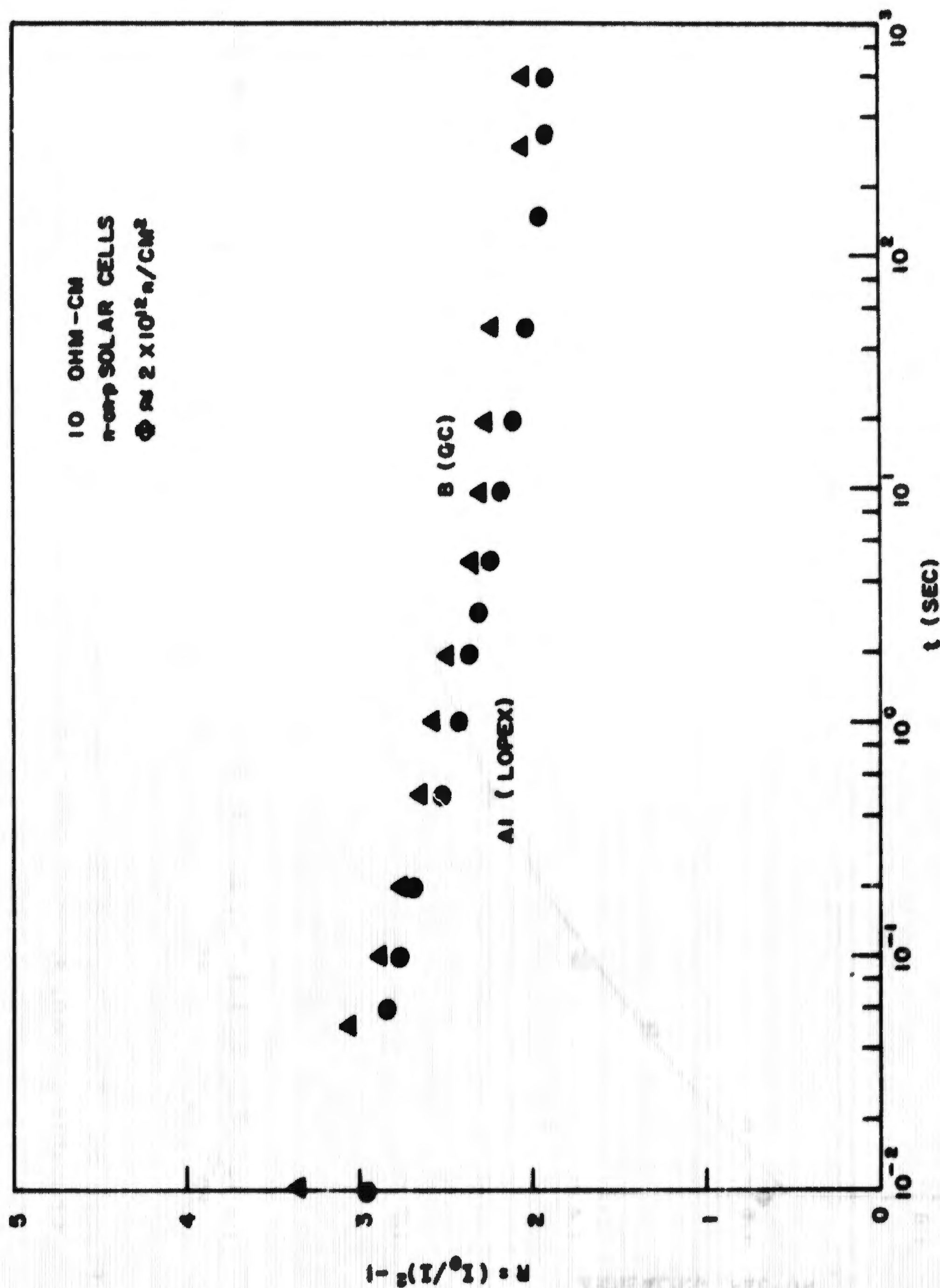

Figure 33. Time dependence of the ratio of radiation-induced to initial recombination center concentration following a 2×10^{12} n/cm^2 pulse for some 10-ohm-cm n-on-p solar cells

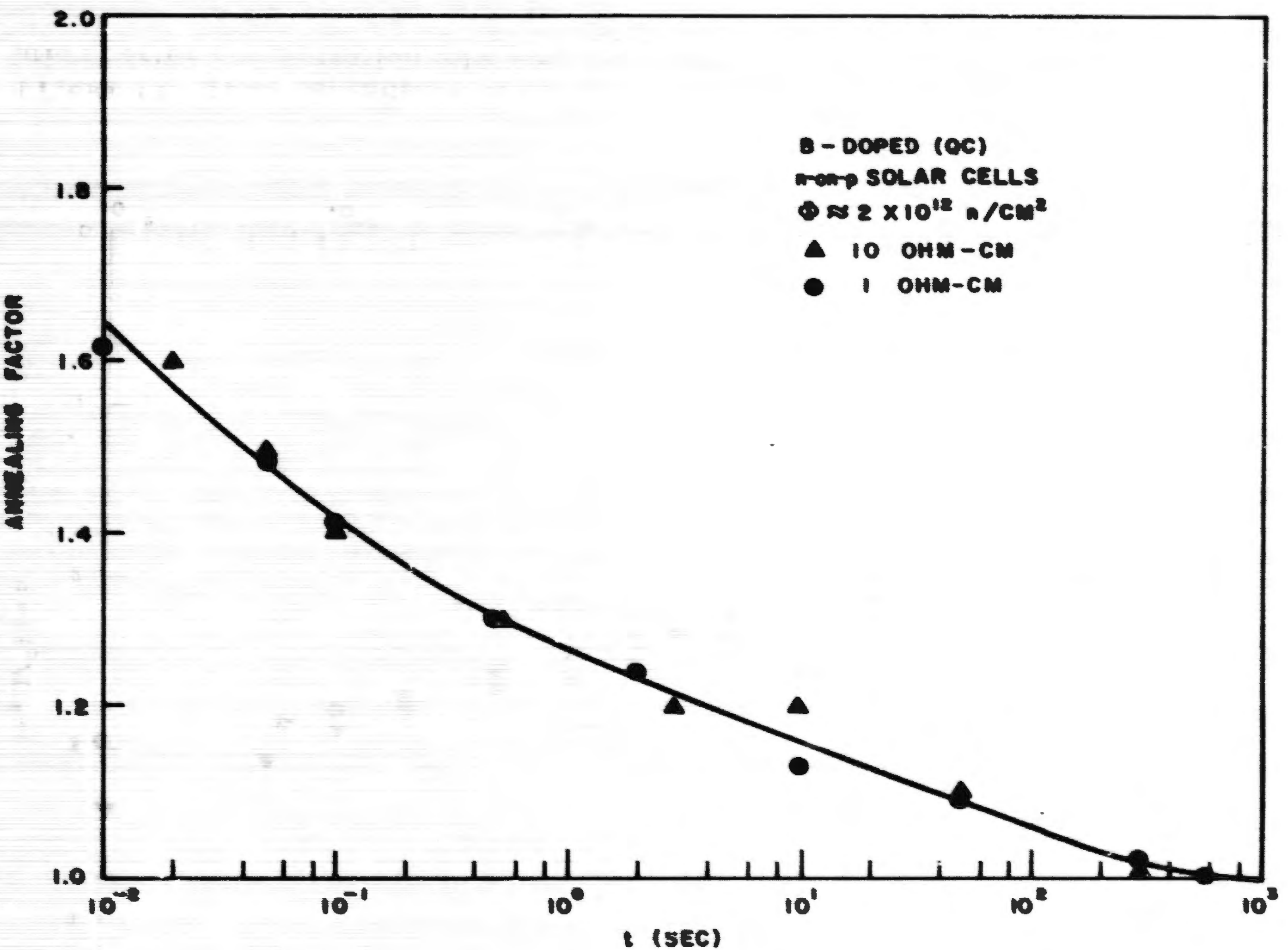

Figure 34. Time dependence of the annealing factor for boron-doped, quartz-crucible-grown, n-on-p solar cells following a 2×10^{12} n/cm^2 pulse

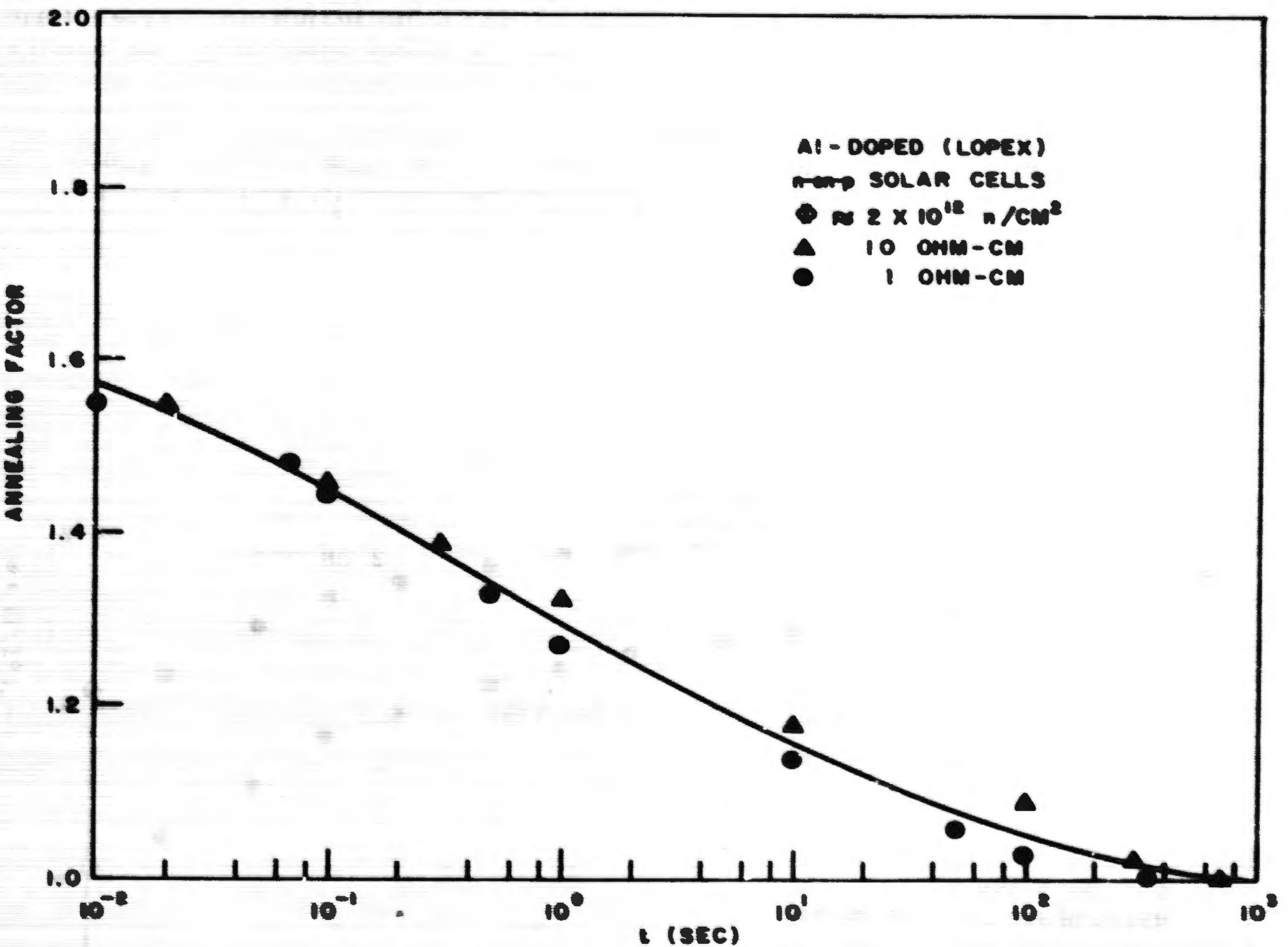

Figure 35. Time dependence of the annealing factor for aluminum-doped, Lopex-grown, n-on-p solar cells following a 2×10^{12} n/cm^2 pulse

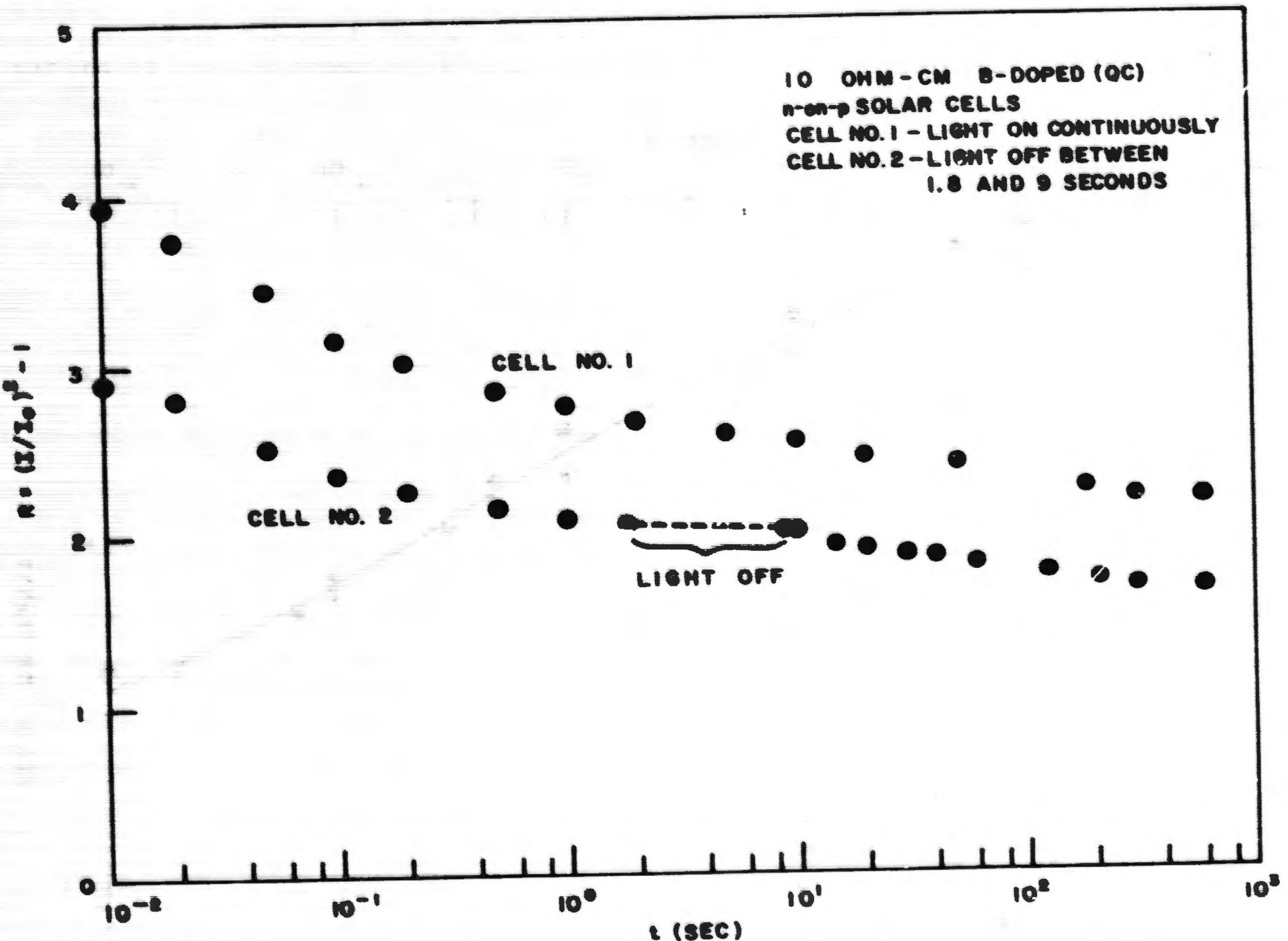

Figure 36. Time dependence of the ratio of radiation-induced to initial recombination center concentration of two 10-ohm-cm, boron-doped, n-on-p solar cells following a 2×10^{12} n/cm^2 pulse, showing the effect on annealing of injection level

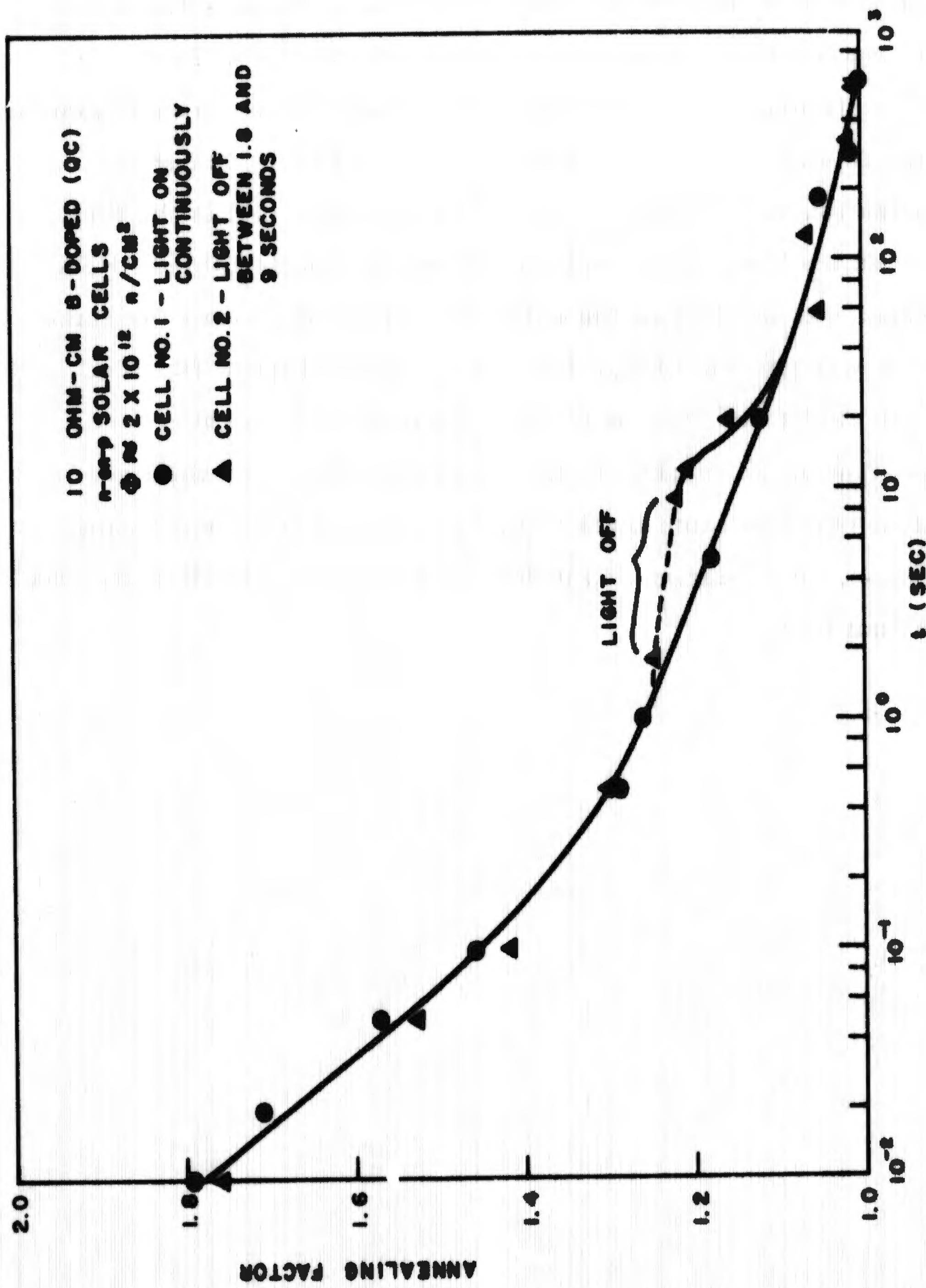

Figure 37. Time dependence of the annealing factor for two 10-ohm-cm, boron-doped, n-on-p solar cells, showing dependence of annealing on injection level

period, but it continued again as soon as the light was turned on.

Preliminary measurements in APFA III have served to point up the principal problem involved in short-term anneal investigations with the time resolution that is theoretically possible with the APFA. This problem is due to ionization in the solar cell caused by the prompt gamma flux from the fission process. The lower trace of Figure 38a shows the effect of ionization on a 10-ohm-cm, boron-doped solar cell in the test apparatus when the Linac beam was pulsed into the unassembled APFA sphere. There was no light on the sample. Figure 38b shows the same signal when it was passed through the gate circuit of Figure 20. The ionization drives the cell into saturation, from which it recovers with the time constant of the lifetime of the base material. With the light on, the cell output is at the same level as that to which it is pinned during the gating pulse, so the large step observed in Figure 38b will be avoided during an actual test.

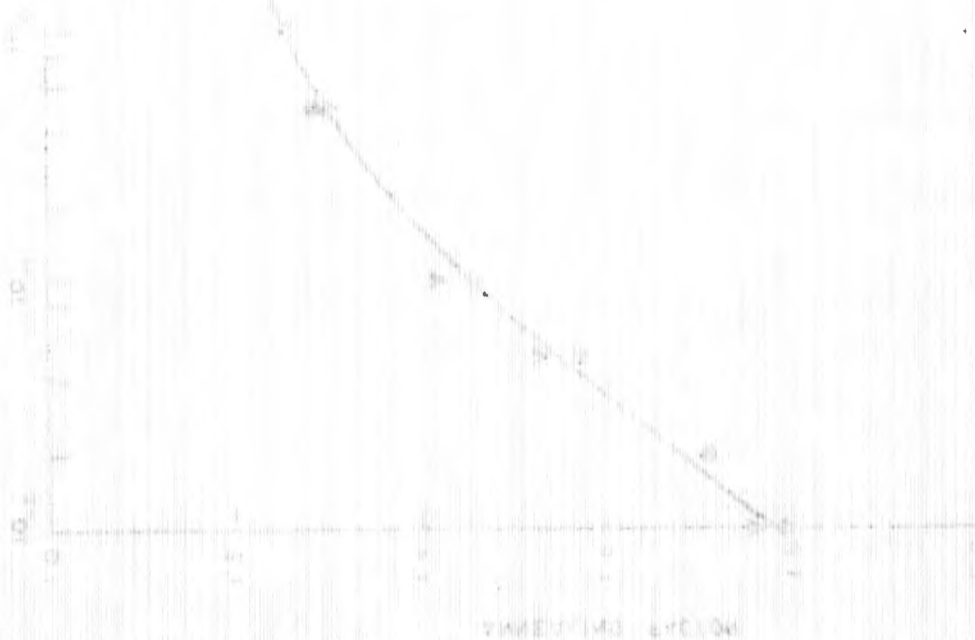

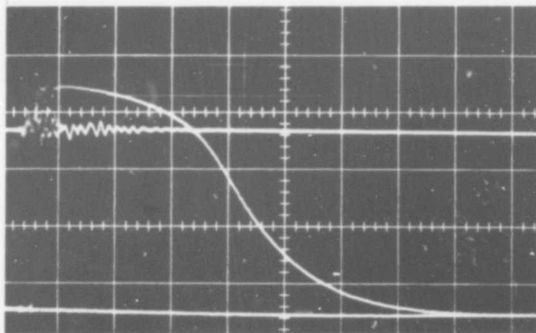

Lower: Solar cell
Gain: 100 mv/div
Sweep: 10 μsec/div

(a) Not gated

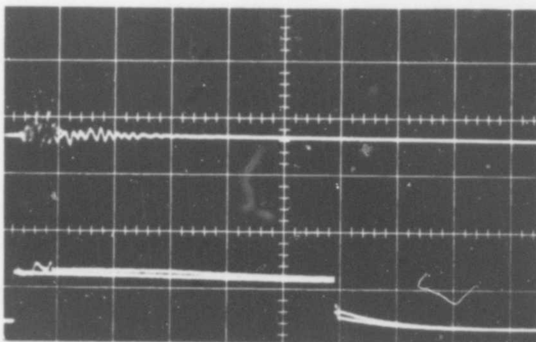

Lower: Solar cell
Gain: 100 mv/div
Sweep: 10 μsec/div

(b) Gated

Figure 38. Solar-cell output with no light on during Linac pulse into unassembled APFA sphere

SECTION VI
DISCUSSION AND SUMMARY

The conductivity anneal data presented in Figure 22 indicate a reverse annealing in conductivity for all types of semiconductor materials. The anneal is stronger in p-type than in n-type material for both germanium and silicon and, at least in the p-type silicon samples tested, is stronger in the higher-resistivity material. There is evidence of a forward-annealing stage following the initial reverse anneal in both of the germanium samples. The strange shape of the 7-ohm-cm n-type silicon data is not understood, although it was duplicated in three separate tests. These experiments add further weight to the argument that short-term annealing is a bulk, rather than surface, phenomenon. When compared with the forward anneal of carrier lifetime, the reverse anneal for the conductivity proves that the annealing process is a rearrangement of defect types, not a defect annihilation such as interstitial-vacancy recombination.

Bulk photoconductivity samples would provide the most likely direct data on lifetime annealing, but measurements on such samples are difficult to make because of the low signal levels obtained for even moderate injection levels. They are further complicated by spurious photovoltages, which are generated at sample contacts and which can be of the same order of magnitude as the signals being measured. The data presented in Figures 23 through 26 show forward annealing in all samples, but it is essentially completed by about 1 sec. It is not understood at this time why the annealing appears to be complete this early in the bulk samples and obviously continues long after this in the solar cells, unless the signals observed in the bulk-sample experiments were due to contact effects and were not bulk properties at all. Further work in this area should utilize better techniques to mask the contacts from the light to minimize these photovoltages.

The data from p-on-n cells shown in Figures 27 through 31 show little forward annealing in the phosphorus-doped material and the 0.1-ohm-cm arsenic-doped cell. There is an appreciable annealing in the 1-ohm-cm and

10-ohm-cm arsenic-doped cells. Thus, we apparently observe a difference of short-term annealing in n-type silicon with variations in the Fermi level (dopant concentration) and possibly a difference with different impurities, although it has been reported (Reference 12) that the overall lifetime degradation is not dependent on these parameters for n-type silicon. One possible way for these two statements to be compatible is for the phosphorus-doped and high-impurity-concentration arsenic-doped cells to have an annealing component that is too fast to have been detected in these TRIGA tests. Another possibility is that the observed differences may be due to variations in injection level between devices. This parameter will have to be more carefully controlled in future experiments.

The data presented in Figures 32 through 35 and in Table VI show that more annealing takes place in p-type material but that there is little difference due to impurity concentration, at least between 1 ohm-cm and 10 ohm-cm material. There also does not seem to be much difference between materials using different dopants and different manufacturing techniques. The apparent difference in the shape of the annealing-factor curves for the boron-doped, QC-grown material and the aluminum-doped, Lopex-grown material may or may not be significant. More data taken at earlier times will be needed to determine this. Even then, if a difference does show up, it will be necessary to decide whether the difference is due to the dopant or to the manufacturing technique.

The difference in annealing between p-on-n and n-on-p cells, which is quite marked in these experiments, was not observed by Sander and Gregory (Reference 9), who reported annealing in both types of solar cells to be similar. However, in a later paper by these authors (Reference 18), the n-on-p cells do show a greater degree of annealing.

The results of a test, which are demonstrated in Figures 36 and 37, in which one sample was illuminated continuously during the annealing period and another was not, confirms the dependence of annealing on injection level. This injection-level dependence has been observed in earlier transistor studies

(Reference 19) and in silicon-solar-cell experiments conducted by Sander and Gregory (Reference 9 and 18).

Although the APFA III Facility is now operable and has been pulsed, there are still improvements that must be made before its full potential can be realized. Many reactivity measurements of different experiment configurations and experimentation with different reflector configurations must be made. A replacement unit for one of the control components must be obtained before it will be allowed to operate to \$0.86 excess reactivity (multiplication of 1000). At present, its use is limited to \$0.32 excess reactivity (multiplication of 220). The linear accelerator is being modified to bring it up to full potential and it is planned that the fourth accelerating stage will be installed by the end of May 1967. When all of the preliminary tests of the APFA Facility have been made, the automatic control equipment installed, and the change-over of the Linac completed, short-term anneal experiments will commence in earnest. Thus far the experiment test circuits have been checked out for noise level and for operation by remote control from the monitor station. In the one test attempted so far, the neutron fluence was too low for meaningful data to be obtained.

The ionization caused by the fission gammas is a serious problem, as shown by the photograph in Figure 38. The lifetime of the undamaged solar cells used thus far is about 30 μsec. The signal shown in Figure 38 is from a cell which had already been partially damaged by repeated pulsing of the unassembled APFA sphere while the sample was mounted in place. Its lifetime is about 15 μsec. Presuming that cells with lifetime as short as . s can be used, anneal data will still be obscured by ionization until 70 or 80 μsec. Although using cells with lifetimes of a couple of microseconds would get around this problem, it would create another problem in that the APFA neutron fluence would then not be high enough to cause great enough changes in the lifetimes so that annealing could be observed. Using a pulsing light only partially gets around this problem as the injected carriers from the light pulses also have to recombine with this characteristic time. However, if anneal data can be obtained

beginning at 100 μsec, it would be two orders of magnitude better time resolution than has been obtained in the TRIGA experiments and a factor of twenty better than data reported in the Sandia work.

SECTION VII
RECOMMENDATIONS FOR FUTURE INVESTIGATIONS

These experiments have established the basis on which future investigations on short-term anneal should proceed and have indicated the direction which these investigations should take. The following recommendations are made:

1. New n-on-p solar cell samples should be obtained in three groups.

   Group 1— Same acceptor-dopant, same manufacturing technique, different carrier concentrations. (For example, boron-doped; QC-grown; 0.1-, 1-, 10-ohm-cm materials.)

   Group 2— Different acceptor-dopants, same manufacturing technique, same carrier concentration. (For example, boron-, aluminum-, and gallium-doped, QC-grown, 10-ohm-cm materials.)

   Group 3— Same acceptor-dopant, same carrier concentration, different manufacturing techniques. (For example, boron-doped, 10-ohm-cm, QC-, FZ-, and Lopex-grown materials.)

Experiments on these three groups of samples should indicate which construction parameters are important in p-type silicon short-term anneal. The same type of test should then be performed on n-type materials.

2. Using the materials which demonstrate the strongest annealing in room-temperature experiments, temperature-dependence experiments should be performed at least down to liquid nitrogen temperature. These studies should produce information of the recombination-center energy levels.

3. Using the same material (as a standard), injection-level dependence should be investigated both at room temperature and at low temper-

ature. These studies will yield data on the effect of charge state of the defects on their stability.

Improved apparatus should be used in future studies, such as a high-frequency chopped light and proper filtering, so that more penetrating light will be used which will generate carriers more uniformly in the material.

This page intentionally left blank.

Appendix
DISCUSSION OF THE ANNEALING FACTOR

A term that has been employed as a measure of annealing in various short-term anneal studies is called the annealing factor. The use of this factor is based on the fact that the number of radiation-induced recombination centers increases linearly with neutron fluence and that minority-carrier lifetime is inversely proportional to the number of recombination centers. This linear relationship holds if the fluence is delivered in a low neutron flux or if the lifetime (or parameter dependent on lifetime) is measured after completion of all short-term annealing. The annealing factor is defined below for various devices:

Bulk lifetime samples

$$A.F. = \frac{\frac{1}{\tau} - \frac{1}{\tau_0}}{\frac{1}{\tau_\infty} - \frac{1}{\tau_0}}$$

Transistors

$$A.F. = \frac{\frac{1}{\beta} - \frac{1}{\beta_0}}{\frac{1}{\beta_\infty} - \frac{1}{\beta_0}}$$

Solar cells

$$A.F. = \frac{\frac{1}{I^2} - \frac{1}{I_0^2}}{\frac{1}{I_\infty^2} - \frac{1}{I_0^2}}$$

The subscript 0 denotes the value of the parameter before irradiation, the subscript ∞ denotes the value of the parameter after all annealing has taken place, and no subscript denotes the value of the parameter as a function of time.

Because of the linear relationship of the lifetime-dependent parameters on neutron fluence, the value of the parameter during any stage in the annealing process may be equated to an effective neutron fluence, Φ^*, the fluence necessary to cause that same value of the parameter when the fluence is delivered in a low neutron flux. The ratio of this effective fluence to the actual fluence is the annealing factor.

Some problems arise in using the annealing factor in comparing the results of different experiments. The annealing factor as a single number for a given device and neutron pulse is the maximum value observed for the factor. Obviously, the value obtained is a function of the time resolution with which the measurements are made. Another difficulty is that the ∞ value of the parameter that is used in the calculation of the annealing factor is seldom the true one, as annealing is still going on after the completion of most measurements. (Curtis (Reference 12) shows annealing continuing even at 6×10^3 sec in both n- and p-type materials.) Therefore, the annealing factor obtained in any experiment is not only dependent on when the measurement starts but also on when it is completed.

The annealing factor is not a valid figure of merit for radiation resistance in devices and is only useful in this regard if the $1/\beta$ versus Φ data are also available. This can be seen in the plots of Figure 39, 40, 41, and 42. From the plot in Figure 40 it can be seen that transistor B is more radiation-resistant than transistor A. Figure 39 shows the annealing behavior of these two hypothetical transistors following a pulse of neutrons. Transistor A demonstrates an annealing factor of 5, whereas transistor B shows an annealing factor of only 2. From this it might be concluded that transistor B, having the smaller annealing factor, is better; thus, a small annealing factor indicates a better transistor. However, consider next the two hypothetical transistors of Figures 41 and 42. Transistor C is identical to transistor A in low-flux neutron degradation

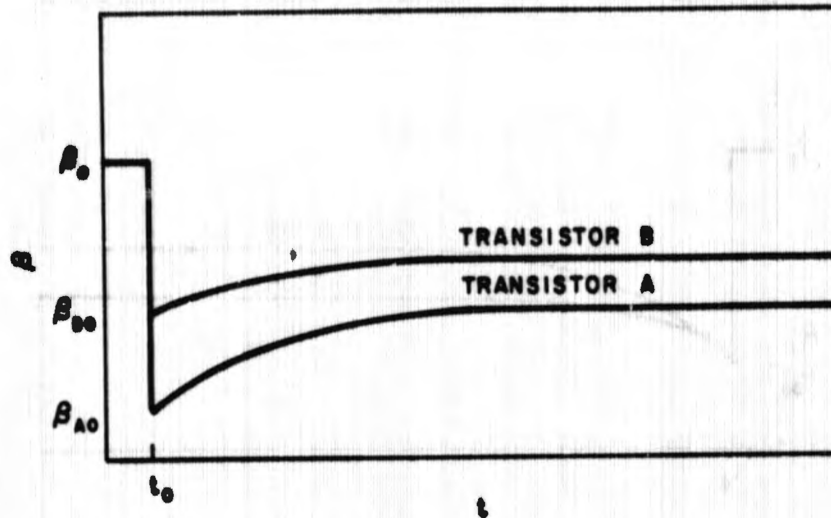

Figure 39. β vs t for two hypothetical transistors, A and B, following a neutron pulse of fluence Φ

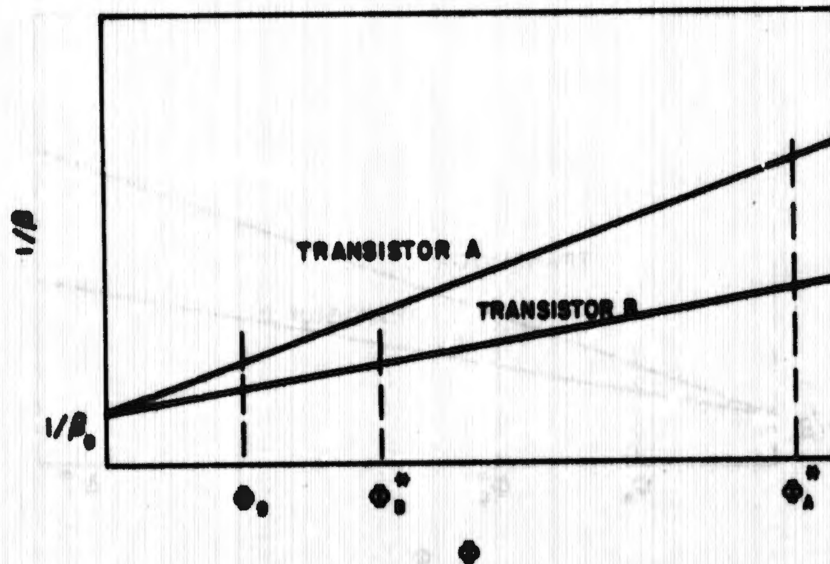

Figure 40. 1/β vs Φ for two hypothetical transistors, A and B, with the fluence delivered in a low neutron flux

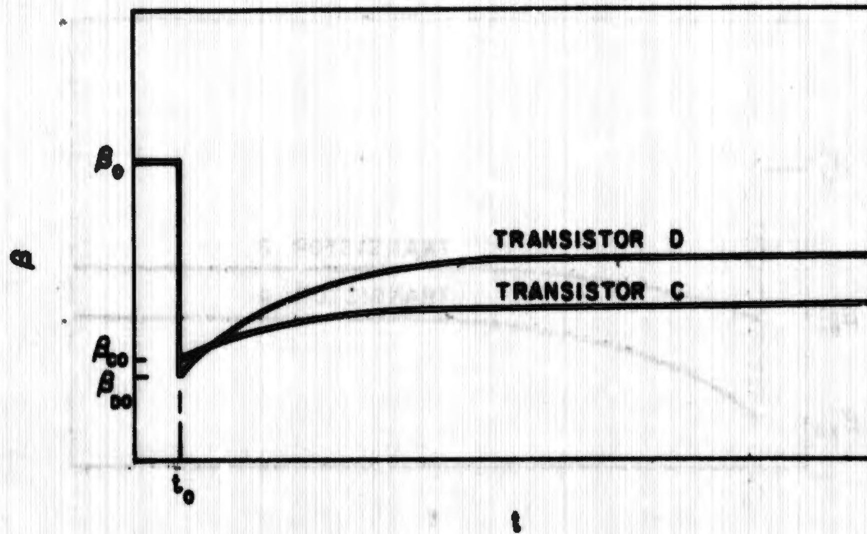

Figure 41. β vs t for two hypothetical transistors, C and D, following a neutron pulse of fluence Φ_0

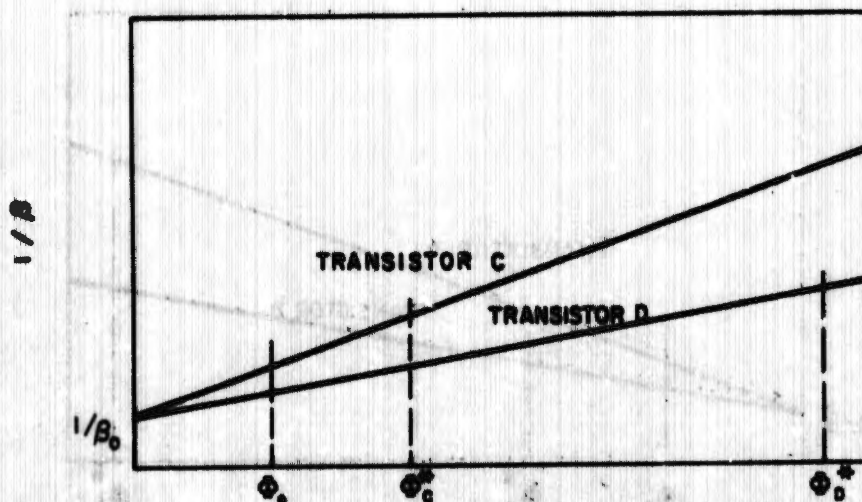

Figure 42. $1/\beta$ vs Φ for two hypothetical transistors, C and D, with the fluence delivered in a low neutron flux

and transistor D is identical to transistor B. Each differs from its counterpart in annealing behavior. Figure 41 demonstrates this difference. The annealing factors are 2 for transistor C and 5 for transistor D. In this case, the more radiation-resistant transistor, D, in terms of final β degradation, has the larger annealing factor. Thus, the annealing factor, by itself, cannot be used to judge the radiation resistance of a transistor.

If used properly in conjunction with the low-flux neutron degradation of reciprocal β data, the annealing factor is quite useful. For example, it would show the circuit designer that even though transistor D of Figures 41 and 42 is a better transistor in terms of β degradation than transistor C, there is a period immediately following a neutron pulse in which transistor C has the higher β. This might make transistor C the better transistor to use in some applications. With proper care in its derivation and use, the annealing factor can prove a useful tool to the design engineer and a proper parameter for evaluating short-term annealing.

REFERENCES

1. Lindhard, J., and M. F. Scharff, Phys. Rev., 124, 1961, p. 128.
2. Hansen, N. E., and S. C. Fulta, University of California, Lawrence Radiation Laboratory, Report UCRL-6099, 1960.
3. Bemski, G., JAP, 30, 1959, p. 1195.
4. Watkins, G. D., et al., JAP, 30, 1959, 1198.
5. Wikner, E. G., and H. Horiye, IEEE Trans. Nuc. Sc., NS-13, 1966, p. 18.
6. Corbett, J. W., and G. D. Watkins, Phys. Rev., 138, 1965, p. A555.
7. Seitz, F., and J. S. Koehler, Solid State Physics, Vol. II, F. Seitz and D. Turnbull, eds., Academic Press, Inc., New York, 1956.
8. Bertolotti, M., T. Papa, D. Sette, and G. Vitali, JAP, 36, 1965, p. 3506.
9. Sander, H. H., and B. L. Gregory, IEEE Trans. Nuc. Sc., NS-13, 1966, p. 53.
10. Baroody, E. M., Phys. Rev., 124, 1961, p. 745.
11. Holmes, D. K., Radiation Damage in Solids, Vol. II (Part of the Proceedings of the Symposium on Radiation Damage in Solids and Reactor Materials held by the International Atomic Energy Agency at the Foundazione Cini, S. Giorgi Maggiore, Venice, 7-11 May 1962; printed by IAEA).
12. Curtis, O. L., Jr., R. F. Bass, and C. A. Germano, Northrup Nortronics Division of North American Corporation, Report ARD/66-56R, Contract DA-49-186-AMC-235(X), Harry Diamond Laboratories, November 1966.
13. Gossick, B. R., JAP, 30, 1959, p. 1214.
14. Christie, E. R., and B. W. Mar, Lawrence Radiation Laboratory, University of California, UCRL-6105, UC-46 TID-4500, 15th ed., 1961.
15. Rosen, L., et al., Los Alamos Scientific Laboratory, Report LA-1670, 1954.
16. Granberg, L., et al., Phys. Rev., 103, 1956, p. 662.
17. Esposito, R. M., et al., JAP, 38, 1967, p. 825.
18. Gregory, B. L., and H. H. Sander (to be published in IEEE Trans. Nuc. Sc.).
19. Sander, H. H., Sandia Corporation, Report SC-R-64-192, July 1964.